The University of Nottingham
UNITED KINGDOM · CHINA · MALAYSIA

Ruhl, Micha and Hesselbo, Stephen P. and Hinnov, Linda and Jenkyns, Hugh C. and Xu, Weimu and Riding, James B. and Storm, Marisa and Minisini, Daniel and Ullmann, Clemens V. and Leng, Melanie J. (2016) Astronomical constraints on the duration of the Early Jurassic Pliensbachian Stage and global climatic fluctuations. Earth and Planetary Science Letters, 455 . pp. 149-165. ISSN 0012-821X

Access from the University of Nottingham repository:
http://eprints.nottingham.ac.uk/38010/1/Ruhl_etal_2016___LIBRARY_SUBMISSION_VERSION.pdf

Copyright and reuse:

The Nottingham ePrints service makes this work by researchers of the University of Nottingham available open access under the following conditions.

This article is made available under the Creative Commons Attribution Non-commercial No Derivatives licence and may be reused according to the conditions of the licence. For more details see: http://creativecommons.org/licenses/by-nc-nd/2.5/

A note on versions:

The version presented here may differ from the published version or from the version of record. If you wish to cite this item you are advised to consult the publisher's version. Please see the repository url above for details on accessing the published version and note that access may require a subscription.

For more information, please contact eprints@nottingham.ac.uk

Earth and Planetary Science Letters 455 (2016) 149–165

Article Info

Article history:
Received 6 April 2016
Received in revised form 24 August 2016
Accepted 27 August 2016
Available online 5 October 2016
Editor: M. Frank

ASTRONOMICAL CONSTRAINTS ON THE DURATION OF THE EARLY JURASSIC PLIENSBACHIAN STAGE AND GLOBAL CLIMATIC FLUCTUATIONS

MICHA RUHL[1], STEPHEN P. HESSELBO[1,2], LINDA HINNOV[3], HUGH C. JENKYNS[1], WEIMU XU[1], JAMES B. RIDING[4], MARISA STORM[1], DANIEL MINISINI[5], CLEMENS V. ULLMANN[2], MELANIE J. LENG[4,6]

[1] Department of Earth Sciences, University of Oxford, South Parks Road, Oxford OX1 3AN, UK
[2] Camborne School of Mines and Environment and Sustainability Institute, University of Exeter, Penryn Campus, Penryn, Cornwall, TR10 9FE, UK
[3] Department of Atmospheric, Oceanic and Earth Sciences, George Mason University, Fairfax Campus, 4400 University Drive, Fairfax, VA 22030, Virginia, USA
[4] British Geological Survey, Keyworth, Nottingham NG12 5GG, UK
[5] Shell Exploration and Production Incorporated, Shell Houston Technology Center, 3333 Highway 6 South, Houston, TX 77082, Texas, USA
[6] School of Geography, University of Nottingham, University Park, Nottingham NG7 2RD, UK

Keywords: *astrochronology, carbon-cycle, cyclostratigraphy, Early Jurassic, Pliensbachian, strontium isotopes*

ABSTRACT

The Early Jurassic was marked by multiple periods of major global climatic and palaeoceanographic change, biotic turnover and perturbed global geochemical cycles, commonly linked to large igneous province volcanism. This epoch was also characterized by the initial break-up of the super-continent Pangaea and the opening and formation of shallow-marine basins and ocean gateways, the timing of which are poorly constrained. Here, we show that the Pliensbachian Stage and the Sinemurian–Pliensbachian global carbon-cycle perturbation (marked by a negative shift in $\delta^{13}C$ of 2–4‰), have respective durations of ~8.7 and ~2 Myr. We astronomically tune the floating Pliensbachian time scale to the 405 Kyr eccentricity solution (La2010d), and propose a revised Early Jurassic time scale with a significantly shortened Sinemurian Stage duration of 6.9 ± 0.4 Myr. When calibrated against the new time scale, the existing Pliensbachian seawater $^{87}Sr/^{86}Sr$ record shows relatively stable values during the first ~2 Myr of the Pliensbachian, superimposed on the long-term Early Jurassic decline in $^{87}Sr/^{86}Sr$. This plateau in $^{87}Sr/^{86}Sr$ values coincides with the Sinemurian–Pliensbachian boundary carbon-cycle perturbation. It is possibly linked to a late phase of Central Atlantic Magmatic Province (CAMP) volcanism that induced enhanced global weathering of continental crustal materials, leading to an elevated radiogenic strontium flux to the global ocean.

[1] INTRODUCTION

The Early Jurassic (201.4–174.1 Ma) is distinguished by the end-Triassic mass extinction and global warming event, climatic cooling in the Late Pliensbachian and subsequent greenhouse warming in the Early Toarcian (McElwain et al., 1999; Hesselbo et al., 2002; Ruhl et al., 2011; Gradstein et al., 2012; Wotzlaw et al., 2014; Gomez et al., 2015; Korte et al., 2015). Continental rifting and the break-up of Pangaea in the Early Jurassic led to the formation of continental and marine rift basins, which acted as major sites of organic carbon burial and led to the generation of hydrocarbon source rocks (Fleet et al., 1987; Olsen, 1997). The equatorial Tethys Ocean was connected in the Early Jurassic (Sinemurian) to Eastern Panthalassa via the Hispanic Corridor and to the high-latitude Boreal realm via the Viking Corridor, likely initiating changes in (global) ocean currents and planetary heat distribution (Figure 1; Porter et al., 2013; Korte et al., 2015).

The Early Toarcian in particular was set apart by the global Toarcian Oceanic Anoxic Event (T-OAE), with possibly the largest exogenic carbon-cycle perturbation in the Mesozoic, and associated perturbations in other global geochemical cycles, palaeoclimate and the palaeoenvironment, linked to emplacement of a large igneous province (LIP) in the Karoo-Ferrar region (Jenkyns, 2010; Burgess et al., 2015; Percival et al., 2015). The Early Jurassic was also marked by multiple somewhat smaller scale fluctuations in the global exogenic carbon cycle (Riding et al., 2013; Jenkyns and Weedon, 2013), shifts between climatic warming and cooling on regional and global scales (Korte et al., 2009; Korte and Hesselbo, 2011; Korte et al., 2015), marine and continental extinction and origination events (Close et al., 2015), and fluctuations in regional and global sea-level (Hallam, 1997; Hesselbo et al., 2004, 2008). The age, rate of change, and duration of these events are, however, poorly constrained and their inter-relationships only crudely appreciated.

Here, we determine the age and duration of the Early Jurassic Pliensbachian Stage and ammonite zones and subzones in the hemipelagic marine sedimentary record of the Mochras Farm (Llanbedr) Borehole from west Wales (Cardigan Bay Basin). The Mochras Borehole represents ~1300 m of possibly the most continuously deposited and stratigraphically expanded Lower Jurassic sedimentary archive known (Figure 2; Hesselbo et al., 2013). High-resolution (sub-precession scale) element concentration data from this cored material are used to construct a floating astronomical time scale for the Early Jurassic Pliensbachian Stage. Combined with published astrochronological and radiometric constraints on the age of the Rhaetian–Hettangian (Triassic–Jurassic) and Pliensbachian–Toarcian Stage boundaries, and astrochronological constraints on the duration of the Hettangian and Toarcian Stages, we calculate the duration and age of the Pliensbachian Stage and its constituent zones. With these data, we then assess the duration and rate of change of the Sinemurian–Pliensbachian climatic and global carbon-cycle perturbations and the Late Pliensbachian climatic cooling cycles, and assess the rate of change of Pliensbachian seawater $^{87}Sr/^{86}Sr$.

[2] THE MOCHRAS FARM (LLANBEDR) BOREHOLE

The Mochras Farm (Llanbedr) Borehole, hereafter referred to as Mochras, was drilled in 1968–1970 on the west coast of Wales (52°48'32" N, 4°08'44" W; Figure 1; Woodland, 1971; Dobson and Whittington, 1987; Hesselbo et al., 2013; Copestake and Johnson, 2014). The borehole yielded, unexpectedly, a ~1.3 km-thick (601.83–1906.78 m below surface), biostratigraphically complete succession of calcareous mudstone and clay-rich limestone, representing almost the complete Early Jurassic, an interval representing some 27 Myr of geological time.

The Early Jurassic age sedimentary record in the Mochras core is more than twice

as thick as any other UK core or coastal outcrop, and it is over four times more expanded than the well-studied Sancerre–Couy core from the Paris Basin, France (Figure 2; Tappin et al., 1994; Hesselbo et al., 2013; Boulila et al., 2014). The Hettangian and Sinemurian part of the Mochras core was largely broken up for ammonite biostratigraphy; hence only limited continuous core is preserved for these stages. Continuous core slabs are, however, preserved for the Pliensbachian and Toarcian parts of Mochras (Hesselbo et al., 2013).

[3] BIO- AND CHEMOSTRATIGRAPHY

Biostratigraphical zones, combined with high-resolution geochemical proxy records, provide the primary means for global correlation of Lower Jurassic marine and terrestrial sedimentary archives. The Pliensbachian Stage in northwest Europe is subdivided into five ammonite zones (and 15 ammonite subzones), which are all present and recognized in the Mochras core (Ivimey-Cook, 1971; Page, 2003; Copestake and Johnson 2014). In this paper, these are referred to as zones and subzones, and are named by the index species name (e.g. *margaritatus* zone). Foraminifers provide further biostratigraphical constraints, and allow detailed correlation to records elsewhere (Copestake and Johnson, 2014).

The Pliensbachian is further marked by perturbations of global geochemical cycles and climate. A 2–4‰ negative shift in the carbon-isotope composition ($\delta^{13}C$) of skeletal (belemnite) calcite, bulk shallow-water carbonate, and organic matter is recognized at the Sinemurian–Pliensbachian boundary at Robin Hood's Bay (Yorkshire, UK), the Central Apennines and Trento Platform (Italy), in Portugal and Germany, and in the Mochras core (Jenkyns et al., 2002; Morettini et al., 2002; van de Schootbrugge et al., 2005; Woodfine et al., 2008; Korte and Hesselbo, 2011; Franceschi et al., 2014). This negative carbon-isotope excursion (CIE) likely represents a global carbon-cycle perturbation and associated climatic change, and allows detailed stratigraphical correlation, potentially at a resolution equivalent to, or even significantly higher than, ammonite zones. The Late Pliensbachian was marked by a major positive shift, of up to 5‰, in the $\delta^{13}C$ of wood ($\delta^{13}C_{WOOD}$), and up to 3‰ in the $\delta^{13}C$ of organic matter ($\delta^{13}C_{TOC}$; TOC: Total Organic Carbon) (Figure 7; Suan et al., 2010; Korte & Hesselbo, 2011; Silva et al., 2011), reflecting enrichment of ^{13}C in the coupled ocean-atmosphere carbon pool, and thus a perturbation of the global carbon cycle. This carbon-cycle perturbation determined from the upper *margaritatus* zone, correlates with regionally identified sea-level fluctuations and associated changes in shallow-marine $\delta^{18}O_{CALCITE}$, possibly reflecting climatic cooling cycles under conditions of massive carbon burial, with an enhanced flux of organic matter from the ocean-atmosphere system to the sedimentary carbon pool (Korte and Hesselbo, 2011). Alternatively, regional cooling may have resulted from an early phase of obstruction of the Viking Corridor, leading to decreased seawater temperatures across northwest Europe (Korte et al., 2015). The observed Pliensbachian perturbations in global geochemical cycles allow for detailed high-resolution stratigraphical correlation between geographically separated sedimentary archives from both the marine and terrestrial realms.

[4] ANALYTICAL METHODS

High-resolution (10–15 cm) elemental concentrations (e.g. Ca, Fe, Ti) were obtained by hand-held X-ray fluorescence (XRF) analyses on the slabbed archive half of the Mochras core, from the Upper Sinemurian *raricostatum* zone to the Lower Toarcian *tenuicostatum* zone (1284.08–861.32 m). Rock-Eval analysis, providing Total Organic Carbon (TOC) content, Hydrogen Index (HI) values and % Mineral Carbon, was performed on ~50 mg of homogenized sample, with the Rock-Eval VI unit from Vinci Technologies, at the

department of Earth Sciences, University of Oxford. Analysis of $\delta^{13}C_{TOC}$ was performed on decarbonated and homogenized Late Pliensbachian age outcrop samples from Staithes (Yorkshire, UK), utilising ammonite biostratigraphy for correlation to the Mochras core (Figure 7). Detailed methodology and data quality control are described in the Supplementary Online Materials.

[5] RESULTS AND DISCUSSION

[5.1] SEDIMENTARY RHYTHMS IN THE PLIENSBACHIAN OF MOCHRAS

The Pliensbachian in the Mochras core shows metre-scale lithological couplets of pale grey limestone and dark brown to grey, locally faintly laminated, mudstone, with individual couplets commonly showing gradual transitions between these end-members (Figure 3). The lithological expression of these couplets does, however, vary, in some cases being represented by calcareous mudstone (commonly also more silty) alternating with locally darker, shaly mudstone. These primary lithological cycles occur throughout the Pliensbachian in the Mochras core and vary in thickness between ~30 cm (e.g. latest Pliensbachian) and ~90 cm (e.g. Early Pliensbachian), with individual carbonate beds measuring 20–40 cm (reduced to 5–20 cm in the Late Pliensbachian) (Figures 3, 4). The lithological couplets are especially pronounced at the Sinemurian–Pliensbachian transition (base *jamesoni* zone) and the top *ibex* to base *margaritatus* zones where they comprise carbonate-poor mudstone with moderate organic-matter content (TOC: ~0.9–2.1%) and carbonate-rich mudstone or limestone ($CaCO_3$: ~10–65%) with reduced organic-matter content (Figures 3, 4; Supplementary Figure 2).

Individual lithological couplets are generally symmetrical in nature, with little indication of depositional hiatus or scouring (Figure 3). The more organic-rich lithology is commonly dark grey and faintly laminated on a millimetre scale, particularly in the lowermost Pliensbachian part of the core, whereas the more carbonate-rich lithology is commonly thoroughly bioturbated (Figure 3). Thin-section analysis shows evidence for early diagenetic processes, such as calcite replacement and cementation (Supplementary Figure 3), possibly resulting from the degradation of organic matter and the associated reduction of sulfate, as evidenced by the occurrence of pyrite framboids. However, we exclude the possibility that the lithological couplets are solely related to diagenesis, and interpret them as depositional in origin, as supported by the burrow mottling, with dark-pale and pale-dark mixing of primary sediments (cf. Hallam, 1986). Furthermore, fluctuations in HI values of the bulk sedimentary organic matter closely match the observed variations in $CaCO_3$, suggesting a climatic control on periodic fluctuations in the supply of organic and inorganic matter to the seabed (Supplementary Figure 2), similar to that observed for the Upper Jurassic Kimmeridge Clay Formation at Kimmeridge Bay (UK) and the Lower Jurassic Blue Lias Formation in southern England (Weedon, 1985; Waterhouse, 1999; Weedon et al., 1999; Clemence et al., 2010; Ruhl et al., 2010). Alternatively, observed drops in HI values may have resulted from the oxidative removal of marine algal organic matter in better-oxygenated conditions in the water column and/or sedimentary pore space.

Lithological couplets of similar character have also been observed for coeval Pliensbachian successions in other marine basins across the UK (e.g. Sellwood, 1970, 1972; van Buchem and McCave, 1989; van Buchem et al., 1992, 1994; Hesselbo and Jenkyns 1995; Weedon and Jenkyns, 1999). For example, lithological changes in the Mochras core closely resemble the time-equivalent Belemnite Marl Member (Charmouth Mudstone Formation) in outcrops on the Dorset coast, southern England, where individual beds and distinct calcareous mudstone-shale couplets are laterally continuous for over 2 km (Hesselbo and Jenkyns, 1995; Weedon & Jenkyns, 1999), suggesting chronostratigraphical significance and a stable allogenic forcing mechanism, likely to be

high-frequency climate change. The latest Sinemurian and Pliensbachian sedimentary sequence in the Mochras core also shows similar periodic alternations in lithology relative to the coeval shallow-marine Redcar Mudstone Formation at Robin Hood's Bay, although these latter sediments are characterized by silty to very fine sandy mudstone beds alternating with silty mudstone and shale, with common levels of concretionary siderite, and which were interpreted to originate from changes in storm frequency (van Buchem & McCave, 1989; van Buchem et al., 1992, 1994; Hesselbo and Jenkyns 1995; van Buchem and Knox, 1998).

[5.2] MILANKOVITCH-CONTROLLED SEDIMENTARY PERIODICITIES IN THE PLIENSBACHIAN OF THE MOCHRAS CORE

The observed decimetre- to metre-scale amplitudinal change in calcium concentration determined by XRF directly reflects the observed lithological couplets (in $CaCO_3$) and is especially prominent around the Sinemurian–Pliensbachian boundary (*raricostatum* and *jamesoni* zones) and in the late Pliensbachian *margaritatus* zone (Figures 3, 4), illustrating a strong modulation by long-term periodicities. Iron (Fe) and titanium (Ti) concentrations in the Mochras core also fluctuate strongly and both are largely negatively correlated with the calcium concentration (Figure 3), suggesting simple sedimentary carbonate dilution. However, different climatic controls on detrital element supply or diagenetic element enrichment may also have affected the carbonate-silicate balance. It is reasonable to conclude that diagenesis exerted some control on the distribution of carbonate, likely enhancing the primary lithological cyclicity inferred from sedimentary structures, trace fossils, and other palaeontological characteristics outlined above. The observed fluctuations in calcium concentrations therefore partly reflect relative changes in the particulate carbonate flux, together with diagenetic effects that also have their origins in a primary palaeoenvironmental cyclicity that may have occurred over Milankovitch time scales.

The XRF-based Ca-concentration data series, combined with the stacked core-photographs allow for the initial visual identification of calcareous beds and associated lithological couplets. These lithological couplets are not evenly spaced, but occur in bundles (E^1) of 4–5 sedimentary rhythms. Within a bundle the more calcareous beds generally thicken up-section and become more pronounced, forming a weakly asymmetric cycle (Figures 3, 4). Generally, four of these smaller bundles (E^1), each consisting of 4–5 lithological couplets, occur in one super-bundle (E^2). The observed couplets, bundles (E^1) and super-bundles (E^2) can generally be recognized throughout the core, but vary in thickness, probably due to minor changes in sedimentation rate (Figure 4). The ratio between the thickness of the couplets, the bundles and the super-bundles is, however, constant, consistent with a stable forcing mechanism, which we interpret as a climatic control operating on Milankovitch frequencies.

The lithological couplets in the coeval Belemnite Marl Member in Dorset are suggested to represent ~21 Kyr precession cyclicity (Weedon & Jenkyns, 1999). Following this interpretation, we assign ~100 and ~405 Kyr eccentricity periodicities to the visually defined bundles (E^1) and super-bundles (E^2) (Figures 3, 4). This procedure allows for independent comparison to Milankovitch periodicities assigned from subsequent spectral and multi-taper analyses. Some of the E^1-bundles are, however, marked by only two lithological couplets that are generally thicker and more carbonate-rich, and which consistently occur only during the minimum between two E^2-bundles (Figure 4). Following the above, they may reflect a change from dominant eccentricity-modulated precessional forcing to obliquity forcing.

[5.3] SPECTRAL & MULTI-TAPER ANALYSES

The XRF elemental data obtained from the Pliensbachian of the Mochras core were manipulated to uniform sample spacing using linear interpolation. For spectral analyses, the series were analyzed with the 3π multi-taper method (MTM) using the Astrochron toolkit (Meyers, 2014; R Package for astrochronology, version 0.3.1), with robust red noise models (Mann and Lees, 1996), and with AnalySeries 2.0.8 (Paillard et al., 1996).
Initial spectral analysis was performed with AnalySeries on a detrended data series (with low band-pass filtering to remove periodicities >150 m). Dominant spectral components (Supplementary Figure 4) were filtered from the data series, and compared to the visually defined precession (lithological couplets) and long-term and short-term eccentricity periodicities (Figure 4). The data-series in the depth domain was subsequently converted into a time series, based on the observed and interpreted dominant ~405 Kyr eccentricity cycle. Low-frequency band-pass filtering was then performed with Astrochron on the raw-data time series to remove long-term trends. High-precision extraction of dominant spectral components (Figure 5, Supplementary Figures 4, 5, 6), with long- and short-term cycles of eccentricity, obliquity and precession, were subsequently extracted with Taner bandpass filtering (Astrochron) and AnalySeries.

The MTM power spectrum estimates of the Ca-concentration in the depth domain show dominance of the >150 m spectral peak (Supplementary Figure 4A). Removal of this long-term trend by high band-pass filtering shows dominant spectral components at ~1, ~1.5, ~2.5, ~5.8 and ~24 m (Supplementary Figure 4B). Lithological observations and visually described changes in Ca-concentrations show a pronounced reduction in thickness of the observed lithological couplets, relative to the underlying Pliensbachian strata, in the upper *margaritatus* and complete *spinatum* zones (Figure 4). Individual couplets, however, continue to be spaced in the observed bundles (E^1) and super-bundles (E^2), and lack any evidence of periodic hiatuses. The reduced thickness of individual couplets, combined with the continued bundling, suggests an overall reduced sedimentation rate in this part of the Mochras core.

Individual MTM power spectra for the uppermost *raricostatum* to lower *margaritatus* and the upper *margaritatus* to lowermost *tenuicostatum* zones (Supplementary Figure 4C, 4D, respectively), show that dominant spectral components occur at different frequencies, but with equal internal ratios suggesting a ~40–60% reduction in sedimentation rate in the latest Pliensbachian and very earliest Toarcian (Supplementary Figure 7). The ~1 and ~0.6 m spectral components in these intervals directly reflect the observed primary sedimentary rhythms, recognized throughout the Pliensbachian of the Mochras core (Figure 4). The observed dominant spectral peaks directly reflect the visually ascribed individual lithological rhythms and bundles (E^1) and super-bundles (E^2) in carbonate predominance, likely representing precession and short- and long-term eccentricity. Using this interpretation, the sedimentary and geochemical time series of the Mochras core can be converted from depth to age. The resulting floating astronomical time scale for the Pliensbachian may also then be tuned to the proposed astronomical solutions for this period (e.g. Laskar et al., 2011), using radiometric tie points.

[5.4] ASTRONOMICAL CONSTRAINTS ON THE DURATION OF THE PLIENSBACHIAN STAGE AND AMMONITE ZONES

The base of the Pliensbachian is formally defined by a mudstone bed in the Pyritous Shale Member (Redcar Mudstone Formation) at Robin Hood's Bay, Yorkshire, UK, marked by the lowermost occurrence of the ammonite species *Bifericeras donovani*; with additional stratigraphical markers including a narrow reversed-polarity magnetozone (at the base of Si-Pl N) and a negative excursion in $\delta^{13}C$ (Hesselbo et al. 2000, Meister et al., 2006; Korte and Hesselbo, 2011). The Pliensbachian Stage is conventionally divided into the lower (Carixian) and upper (Domerian) substages and, at a higher resolution, into

ammonite zones. Some authors, e.g. Page (2004), prefer to treat ammonite-based subdivisions as chronozones rather than biozones or zones but, given the absence of corroboration of their time significance, we treat them here as conventional biostratigraphical units. These are successions of sedimentary rock characterised by specific fossil assemblages, and defined to be (closely) approximate in depositional age and hence are characteristic of discrete time intervals.

The visual core observations and interpretations, combined with the spectral and multi-taper analyses of geochemical records, together with the precise biostratigraphical subdivision of the Mochras core, can be used to estimate the duration of Pliensbachian ammonite zones. The precision of the estimates obtained for ammonite zone durations depends on (1) the correct recognition of the dominant orbital signals, and (2) the uncertainty of the precise position of the stratigraphical base of an ammonite zone in the core. Here, we derive ammonite zone durations based on the observed 405 and ~100 Kyr forcing in the geochemical proxy-records. The stratigraphical occurrences of ammonite genera identified in the Upper Sinemurian to Lower Toarcian sections of the Mochras core, which are used to define the ammonite zones, is given in Supplementary Figure 7.

Ammonite zones at Mochras are recognized on the basis of occurrences of characteristic ammonite taxa within the core. Where ammonites are absent between the highest occurrence of one stratigraphically significant taxon and the lowest occurrence of another there is inevitably some uncertainty in the position of the biozone boundary (such range uncertainty for Mochras is indicated diagrammatically in Supplementary Figure 7 and Table 1). Given the above, resulting ammonite biozone durations are estimated at ~2.7 Myr (*jamesoni*), ~1.8 Myr (*ibex*), ~0.4 Myr (*davoei*), ~2.4 Myr (*margaritatus*) and ~1.4 Myr (*spinatum*), yielding a duration of the complete Pliensbachian Stage of ~8.7 Myr (Figure 4; Table 1).

The durations estimated here for the *jamesoni* and *ibex* zones are significantly longer than previous (minimum) estimates from the Belemnite Marl Member (Dorset) and the Ironstone Shale (Yorkshire) (van Buchem et al., 1994; Weedon & Jenkyns, 1999). The base and top of the Belemnite Marl Member (representing the base of the *jamesoni* ammonite zone and the top of the *ibex* ammonite zone in the Dorset outcrops) are marked by stratigraphic gaps (Hesselbo and Jenkyns, 1995; Weedon and Jenkyns, 1999), likely explaining their shorter estimated durations. Equally, the Ironstone Shale in Yorkshire shows strong evidence for condensation at the top of the *jamesoni* zone and within the *ibex* zone (Hesselbo and Jenkyns 1995, 1998; van Buchem and Knox, 1998).

The likely underestimated durations of Early Pliensbachian ammonite zones based on the Belemnite Marl Member sedimentary succession, are furthermore suggested by time series analyses of the Mochras % Ca data imposed onto the Belemnite Marl Member Early Pliensbachian time scale (Supplementary Figure 8), which shows spectral peaks that have no correspondence to dominant astronomical frequencies as known from the geological record and astronomical solutions (Supplementary Figure 8). The new duration estimated here for the *davoei* zone is similar to an earlier proposed value from Breggia Gorge in southern Switzerland, which was previously considered to be only 46% complete (Weedon, 1989). The latter was, however, based on the assumption that Jurassic ammonite zones were ~1 Myr in duration and that only 22 of the expected 48 precession cycles could be recognized (Weedon, 1989). Given the similar duration obtained for the *davoei* zone in the Mochras core, where no evidence for a hiatus, condensation, or non-deposition has been observed, we argue that the *davoei* zone in the Breggia Gorge section is probably complete. The estimated durations of the *margaritatu*s and *spinatum* zones are significantly longer, respectively 0.7 and 0.6 Myr, compared to previous minimum estimates of Weedon (1989) and Weedon and Jenkyns (1999). Our

estimated duration of ~3.8 Myr for the combined *margaritatus*–*spinatum* ammonite zones does, however, closely resemble previous estimates of ~3.96 Myr based on the assumed rate of change of Early Jurassic seawater $^{87}Sr/^{86}Sr$ (McArthur et al., 2000). This does, however, not infer that a linear change in $^{87}Sr/^{86}Sr$ likely occurred throughout the Pliensbachian Stage. A recent estimate on the duration of the Pliensbachian Stage and ammonite zones, with a stage duration of 8.1 Myr, does a-priori assume such linear change for all, but the *jamesoni* zones (McArthur et al., 2016). Such assumption is not necessarily correct, as the rate of change in the $^{87}Sr/^{86}Sr$ ratio of seawater can adjust on multiple time-scales in response to a change in global climate and associated continental (silicate) weathering rates, with a change in the flux of radiogenic $^{87}Sr/^{86}Sr$ to the global oceans, relative to the dominant long-term unradiogenic marine hydrothermal/basalt weathering Sr flux (see also section 5.7).

[5.5] TOWARDS AN ABSOLUTE TIME SCALE FOR THE EARLY JURASSIC HETTANGIAN TO PLIENSBACHIAN STAGES

Zircon U-Pb radiometric dating of the earliest Central Atlantic Magmatic Province (CAMP) flood basalts in eastern North America anchor the end-Triassic mass extinction at 201.56 ± 0.02 Ma, and volcaniclastic material in the Pucara Basin of Peru, indicates an age of 201.51 ± 0.15 Ma for the same event (Schoene et al., 2010; Blackburn et al., 2013; Wotzlaw et al., 2014). The age of the Triassic–Jurassic boundary is radiometrically constrained at 201.36 ± 0.17 Ma in the Pucara Basin (Schaltegger et al., 2008; Schoene et al., 2010; Wotzlaw et al., 2014) and astrochronologically constrained at 201.42 ± 0.02 Ma in the Newark/Hartford succession (Blackburn et al., 2013).

The duration of the Hettangian Stage has been previously estimated by cyclostratigraphy at >~1.29 Myr from the relatively incomplete marine Blue Lias Formation succession in Dorset and Devon, SW England, or at ~2.86 Myr based on an assumed constant linear Early Jurassic decrease in seawater $^{87}Sr/^{86}Sr$ ratios (Weedon and Jenkyns, 1999). More recent estimates for this stage suggest a duration of ~1.7–1.9 Myr, based on the astronomical interpretation of periodically occurring laminated black shales and systematic fluctuations in organic and inorganic geochemical proxy records in the relatively expanded Blue Lias Formation of Somerset, SW England (Ruhl et al., 2010; Hüsing et al., 2014). This duration is further supported by palaeomagnetic correlation to the Geomagnetic Polarity Time Scale (GPTS) of the Newark Basin, USA (Hüsing et al., 2014), and a 199.43 (±0.10) Ma $^{238}U/^{206}Pb$ age for the earliest Sinemurian in the Pucara Basin (Schaltegger et al., 2008; Guex et al., 2012). The duration of the Sinemurian Stage was relatively poorly constrained at ~7.62 Myr, based on assumed constant sedimentation rates and a linear decrease in $^{87}Sr/^{86}Sr$ (Weedon and Jenkyns, 1999).

Acknowledging recognized depositional gaps, earlier astrochronological analyses of the Pliensbachian in Dorset and Yorkshire (UK) and Breggia Gorge (Switzerland), suggested a minimum Pliensbachian Stage duration of 4.82 Myr (Weedon and Jenkyns, 1999); adjustment of these data to an assumed linear decrease in seawater $^{87}Sr/^{86}Sr$ of 0.000042 per Myr for the Belemnite Marl Member, lengthened this minimum duration of the Pliensbachian Stage to ~6.67 Myr (Weedon and Jenkyns, 1999). The $^{87}Sr/^{86}Sr$-based estimate of a ~3.96 Myr long, combined *margaritatus* and *spinatum* zone duration (McArthur et al., 2000), would suggest a much longer duration for the complete Pliensbachian Stage.

Absolute age constraints for the base Toarcian are relatively weak. U-Pb radiometric dating of Lower Jurassic volcanic ashes from the North American Cordillera, integrated with ammonite biochronology, gives ages of 185.7 +0.5/–0.6 Ma for the base of the *kunae* zone (which slightly predates the base of the European *margaritatus* ammonite zone), 184.1 +1.2/–1.6 Ma for the base of the *carlottense* zone (which is

equivalent to the European *spinatum* ammonite zone), 183.6 +1.7/–1.1 Ma for the base of the *kanense* zone (which represents the Pliensbachian–Toarcian boundary and which is equivalent to the combined European *tenuicostatum* and *falciferum* ammonite zones), 182.0 +3.3/–1.8 Ma for the base of the *planulata* zone (which is equivalent to the European *bifrons* ammonite zone), and 181.4 ±1.2 Ma for the base of the *crassicosta* zone (which slightly post-dates the onset of the European *variabilis* ammonite zone) (Pálfy and Smith, 2000). Furthermore, a Re-Os isochron age based on several combined stratigraphical levels in the *falciferum* ammonite zone of the Jet Rock (Yorkshire, UK) suggests an age of 178 ±5 Ma for this time interval (Cohen et al., 2004). The methodological uncertainty on these earlier U-Pb and Re-Os radiometric dates is, however, relatively large, and much larger than one would ideally use for creating tie-points in a floating astrochronological time scale.

A bentonite at the base of the *falciferum*-equivalent ammonite zone (*levisoni*-equivalent ammonite subzone) in the Pucara Basin (Peru) was more recently radiometrically (U-Pb) dated at 183.22 ± 0.25 Myr (Sell et al., 2014). The relatively scarce ammonite occurrences in this section, combined with the bio- and chemostratigraphical uncertainty in correlation to the European realm (Guex et al., 2012), however, do also pose a problem for firmly anchoring the Early Toarcian zones to the numerical time scale. For now, these data, however, provide the basis for the least uncertain age estimate for this time interval, and are therefore used here to anchor the top of the Pliensbachian to the numerical time scale (Figure 6).

The *falciferum* ammonite zone follows the lowest Toarcian *tenuicostatum* zone in northwest Europe and the age-equivalent *polymorphum* zone in the Lusitanian Basin of Portugal. The duration of the *polymorphum* (and *tenuicostatum*) ammonite zone was astrochronologically constrained to 600–900 Kyr at Peniche in the Lusitanian Basin (Suan et al., 2008; Huang and Hesselbo, 2014; Ruebsam et al., 2014, 2015), to ~550 Kyr in the Lorraine Sub-Basin, France, and to a significantly shorter duration of 90–500 Kyr in the Sancerre core of the Paris Basin, France (Boulila et al., 2014). The large range in the Sancerre estimate primarily derived from biostratigraphical uncertainty on the exact position of the lowermost Toarcian in that core. Furthermore, the Lower Toarcian sedimentary record in the Lorraine Sub-Basin and especially also in the Paris Basin is marked by stratigraphical condensation, possibly in response to coeval sea-level change, which compromises the reliability of astrochronological constraints for this time interval, based on the sedimentary successions of these two depocentres (Boulila et al., 2014; Ruebsam et al., 2014, 2015). Assuming (1) the 183.22 ± 0.25 Myr radiometric age for the base of the *falciferum* zone in the Pucara Basin, Peru (Sell et al., 2014), (2) a synchronous age for the *tenuicostatum–falciferum* zonal boundary in north-western Europe, the *kanense–planulata* zonal boundary in South America, and the *polymorphum–levisoni* zonal boundary in the Lusitanian Basin, and (3) a ~600 ± 150 Kyr duration for the *polymorphum* (*tenuicostatum*) zone, a 183.8 ± 0.4 Ma age can, tentatively, be assigned to the base of the Toarcian (Figure 6).

The duration of the combined Toarcian *tenuicostatum* and *falciferum* zones is currently much debated, with estimates ranging from ~1.9 Myr (Suan et al., 2008), to ~1.4 or 2.4 Myr (Kemp et al., 2011), ~2.5 Myr (Huang and Hesselbo, 2014), ~1.54–1.71 Myr (Boulila et al., 2014) and >1.8 Myr (Ruebsam et al., 2014, 2015), depending primarily on differences in the precession versus obliquity versus eccentricity interpretation of astronomically forced steps in the Early Toarcian carbon-isotope ($\delta^{13}C$) and other geochemical proxy records. Seawater $^{87}Sr/^{86}Sr$-based estimates for this time interval suggested a duration of ~1.694 Myr (McArthur et al., 2000), but this figure is problematic because of large-scale tectono-climatic events over this time interval that may have

significantly varied Sr fluxes from both mantle and continental sources, and because of a distinctly European epicontinental data bias.

The radiometrically constrained age of 199.43 ± 0.10 Ma for the base-Sinemurian and the 183.8 ± 0.4 Ma age assigned here for the base Toarcian, suggest a ~15.6 Myr duration for the combined Sinemurian and Pliensbachian Stages (Schaltegger, 2008; Schoene, et al., 2010; Guex et al., 2012). In conjunction with the ~8.7 Myr duration of the Pliensbachian Stage estimated here, we suggest that the Sinemurian Stage was ~700 Kyr shorter than previously estimated and had a duration of 6.9 ± 0.4 Myr, with a 192.5 ± 0.4 Ma age for the base-Pliensbachian (the ± 0.4 Ma uncertainty derives from the combined radiometric and astrochronological uncertainty on the age of Early Toarcian ash-beds in Peru and the duration of the Early Toarcian *tenuicostatum* zone, respectively) (Figure 6; Table 1).

An astronomically calibrated absolute time scale has been constructed successfully for the Neogene and part of the Paleogene (Hilgen et al., 2014). Astronomical solutions for the geological past, however, become increasingly uncertain, especially before ~50 Ma, due to multiple secular resonances in the inner solar system, and in particular with respect to the θ argument ($\theta = (s_4 - s_3) - 2(g_4 - g_3)$, where g_3 and g_4 are related to precession of the perihelion and s_3 and s_4 are related to precession of the node of Earth and Mars) (Laskar et al., 2004, 2011). The 405 Kyr eccentricity cycle, related to the $(g_2 - g_5)$ argument, which reflects the motions of the orbital perihelia of (gravitational pull between) Jupiter and Venus, however, remained relatively stable over the past 250 Myr (Laskar et al., 2004). Different solutions for the 405 Kyr periodicity show a maximum deviation of 2π over 250 Myr, corresponding to a maximum error of <350 Kyr at 200 Ma (Laskar et al., 2004, 2011). The 405 Kyr eccentricity solution, combined with precise radiometric anchor points, can therefore be used as a target curve for the astronomical tuning of floating astronomical time scales, potentially even back into the Mesozoic.

Precise radiometric and astrochronological age constraints for the base of the Hettangian and the base of the Sinemurian potentially allow the Hettangian floating astronomical time scales to be accurately anchored to the stable 405 Kyr eccentricity solution (La2010d) of Laskar et al. (2011) (Figure 6). However, given the radiometric and astrochronological uncertainties for the age of the base-Toarcian, and with that the age of the base-Pliensbachian, we are presently unable to uniquely anchor the Pliensbachian floating astronomical time scale obtained here to the absolute (numerical) time scale and 405 Kyr astronomical solution of Laskar et al. (2011). We therefore propose 3 different models, Options A, B and C (Figure 6). Option-A represents the solution with the youngest base Jurassic and oldest base Toarcian, Option-B represents the solution with the oldest base Jurassic and youngest base Toarcian, and Option-C represents the intermediate case (Figure 6). Importantly, different solutions for the 405 Kyr periodicity show a maximum deviation of <350 Kyr in the Early Jurassic (Laskar et al., 2004), which adds additional uncertainty to this tuning. Consequently, it is currently not possible to assign with confidence particular observed peaks in the proxy records to either the maxima or minima of the 405 Kyr eccentricity cycle.

Astronomically forced changes in bed thickness in the Early Jurassic pelagic chert sequences from the Panthalassic Ocean (Inuyama, Japan) show also dominant precession and short and long eccentricity periodicities (Ikeda and Hori, 2014; Ikeda and Tada, 2014). The end-Triassic mass extinction event and the Pliensbachian–Toarcian boundary are well constrained in these successions, with radiolarian biostratigraphy allowing biostratigraphical correlation with North American and European ammonite zones (Hori, 1990, 1992, 1997). Interestingly, the number of recognised ~405 Kyr eccentricity cycles across the Hettangian to Pliensbachian stages in the Inuyama chert sequence

directly match the number of 405 kyr eccentricity cycles suggested here for this time-period (Option C, Figure 6). Although the Hettangian–Sinemurian and Sinemurian–Pliensbachian boundary are biostratigraphically not very well constrained in the Inuyama chert sequences, Early Jurassic high-resolution astrochronological correlation may be possible between the pelagic and the continental margin realms of the Panthalassa Ocean and the western Tethys, respectively.

[5.6] RATE AND DURATION OF PLIENSBACHIAN CLIMATIC AND GLOBAL CARBON-CYCLE CHANGE

The Early Jurassic was marked by large perturbations in global geochemical cycles, palaeoclimate and the palaeoenvironment, especially at the Triassic–Jurassic transition and in the Early Toarcian (Hesselbo et al., 2002; Jenkyns, 2003, 2010; Korte et al., 2009; Korte and Hesselbo, 2011; Ruhl et al., 2011; Suan et al., 2011; Ullmann et al., 2014; Brazier et al., 2015; Krencker et al., 2015; Al-Suwaidi et al., 2016; and many others).

Recent studies show that the Pliensbachian Stage was also marked by major perturbations in the global carbon cycle and possibly (global) climate. The Early Pliensbachian *jamesoni* zone is marked by a negative shift in $\delta^{13}C$ (of 2–4‰) in marine calcite and organic matter (Jenkyns et al., 2002; van de Schootbrugge et al., 2005; Woodfine et al., 2008; Korte and Hesselbo, 2011; Armendariz et al., 2012; Franceschi et al, 2014; Korte et al., 2015). This shift is also seen in the $\delta^{13}C$ of wood, reflecting global atmospheric change and a rearrangement of the global exogenic carbon cycle, possibly by the release of isotopically depleted carbon into the ocean-atmosphere system (Korte and Hesselbo, 2011). The Late Pliensbachian *margaritatus* zone (*subnodosus* and *gibbosus* subzones) is further marked by a distinct positive shift in $\delta^{13}C$ of marine and terrestrial organic matter, marine calcite and wood (Jenkyns and Clayton, 1986; van de Schootbrugge et al., 2005; Suan et al., 2010; Korte and Hesselbo, 2011; Silva et al., 2011), possibly linked to enhanced carbon burial under favourable marine redox conditions (Hesselbo and Jenkyns, 1995; Suan et al., 2010; Korte and Hesselbo, 2011; Silva et al., 2011; Silva and Duarte, 2015). Possible changes in Pliensbachian atmospheric pCO_2, based on carbon-isotope and leaf stomatal index data, may have affected regional and/or global temperatures (Suan et al., 2008, 2010; Korte and Hesselbo, 2011; Armendariz et al., 2013; Steinthorsdottir and Vajda, 2013; Silva and Duarte, 2015).

The tuned astrochronological time scale for the Pliensbachian presented here, suggests that the Early Pliensbachian negative CIE had a duration of ~2 Myr, possibly linked to a recurrent phase of CAMP magmatism (see also section 5.7; Figures 7, 8). The Late Pliensbachian (upper *margaritatus* zone) $\delta^{13}C$ positive excursion coincided with significant sea level fluctuations, possibly in synchrony with decreasing shallow-marine benthic temperatures (Hesselbo et al., 2008; Korte and Hesselbo, 2011). The Late Pliensbachian (upper *margaritatus* zone) positive carbon-isotope excursion has an estimated duration of ~0.6 Myr (Figure 7).

[5.7] CAMP VOLCANISM AND THE EARLY JURASSIC STEPPED $^{87}Sr/^{86}Sr$ RECORD

Seawater $^{87}Sr/^{86}Sr$ ratios and strontium fluxes to the oceans are controlled by hydrothermal circulation at mid-ocean ridges and other types of basalt-seawater interaction, the continental weathering of silicates, and the dissolution of carbonates, while the fluxes out of the ocean are primarily regulated by carbonate burial (Burke et al., 1982; Elderfield, 1986; Jones et al. 1994a, b; Steuber and Veizer, 2002; Allègre et al., 2010; Krabbenhöft et al., 2010; Ullmann et al., 2013). Changes in seawater $^{87}Sr/^{86}Sr$ ratios can therefore be explained by the change in the relative importance of continental weathering, or a change in the Sr-isotopic composition of the weathering flux, and

564 hydrothermal inputs of Sr into the oceans. The global unradiogenic strontium flux from
565 hydrothermal venting and weathering of fresh ocean-crust along mid-ocean ridges and
566 around island arcs, is probably relatively stable over shorter time scales, but may have
567 varied on tectonic time scales, with changes in the rate of ocean-crust formation along
568 mid-ocean ridge systems and changes in the global extent of spreading ridges and ocean
569 island arcs (Allègre et al., 2010; Van der Meer et al., 2014). The global unradiogenic Sr-
570 flux may also have varied on long (>Myr) Milankovitch periodicities, possibly in
571 response to eustatic sea-level change and changing mid-ocean ridge spreading rates
572 (Cohen and Coe, 2007; Crowley et al., 2015).
573 In the Early Jurassic, seawater $^{87}Sr/^{86}Sr$ ratios show an overall decrease over ~20
574 Myr towards unradiogenic values, from ~0.70775 to ~0.70705 (Jones et al., 1994a;
575 Cohen and Coe, 2007). Proto-Atlantic rifting at this time initiated on the continents, but
576 continued throughout the Jurassic as mid-ocean ridge activity. Increased mid-ocean ridge
577 spreading rates and/or the increased global extent of mid-ocean spreading ridges,
578 combined with the possible increased formation of island arcs, may have provided an
579 enhanced unradiogenic strontium flux to the global oceans (Van der Meer et al., 2014),
580 leading to the observed steady decrease in Early Jurassic seawater $^{87}Sr/^{86}Sr$ up to the
581 Pliensbachian–Toarcian boundary (Jones et al., 1994a, b; Jenkyns et al., 2002). A decline
582 in seawater $^{87}Sr/^{86}Sr$ may alternatively be explained by a decrease in the overall
583 continental weathering flux. However, in the absence of a major orogeny in the Early and
584 Middle Jurassic, the $^{87}Sr/^{86}Sr$ ratio of the global weathering flux probably remained
585 relatively stable (Jones et al., 1994b). The changing style of biomineralization shown by
586 the evolutionary adoption of calcite in Jurassic calcifying organisms, and increasing
587 pelagic calcite production, probably did not play a major role in the observed change in
588 seawater chemistry because seawater Sr/Ca ratios changed in parallel with Sr-isotope
589 ratios, indicating a likely common weathering and/or tectonic origin for both (Ullmann
590 et al., 2013).
591 The base Jurassic Hettangian Stage, however, contrasts in being marked by a ~2
592 Myr plateau, with relatively stable $^{87}Sr/^{86}Sr$ ratios of ~0.70775 (Cohen and Coe, 2007),
593 suggesting the balancing of the unradiogenic Sr flux from basalt-seawater interaction, by
594 supply of radiogenic Sr from the weathering of old continental crust. This period was
595 also marked by major flood-basalt emplacement, with the onset of CAMP volcanism in
596 the latest Triassic, coeval with the end-Triassic mass extinction, at ~201.4 Ma. Its onset
597 preceded the Triassic–Jurassic boundary, defined by the first occurrence of the Jurassic
598 ammonite species *Psiloceras spelae (tirolicum)* (and *Psiloceras spelea (spelae)*), by 100–200 Kyr
599 (Marzoli et al., 1999; Hesselbo et al., 2002; Deenen et al., 2010, 2011; Ruhl et al., 2010;
600 Schoene et al., 2010; Whiteside et al., 2010; Ruhl and Kürschner, 2011; Blackburn et al.,
601 2013; von Hillebrandt et al., 2013; Dal Corso et al., 2014; Hüsing et al., 2014).
602 Astrochronological and radiometric dating constrain emplacement of the major CAMP
603 flood-basalt pulses in the eastern North American Newark, Culpeper, Hartford and
604 Deerfield basins, the Canadian Fundy Basin, the Algarve in Portugal, the Moroccan
605 Argana Basin and the Moroccan High Atlas Mountains, within a relatively short period
606 of time, possibly within 1 Myr after its onset (Olsen et al., 2003; Deenen et al., 2010,
607 2011; Marzoli et al., 2011; Fernandes et al., 2014). The chemical weathering of juvenile
608 basaltic rocks from CAMP is, however, unlikely to have been directly responsible for
609 stabilizing the Hettangian seawater $^{87}Sr/^{86}Sr$ signal, because Sr-isotope values of fresh
610 Large Igneous Province basalts (with values of 0.704–0.706), are much less radiogenic
611 than ambient Early Jurassic seawater (Cohen and Coe, 2007).
612 The release of volcanogenic CO_2 and biogenic and thermogenic methane from
613 sea-floor clathrates and subsurface organic-rich facies following CAMP flood-basalt
614 emplacement and dyke and sill intrusions (Hesselbo et al., 2002; Korte et al. 2009; Ruhl

et al., 2011; Schaller et al., 2011), combined with enhanced greenhouse-gas-induced elevated hydrological cycling (Ruhl et al., 2011; Bonis and Kürschner, 2012), may have enhanced the global weathering of crustal silicates, carbonates and evaporates, and the consequent flux of more radiogenic Sr to the global oceans (Jones and Jenkyns, 2001; Cohen and Coe, 2007).

CAMP-attributed flood-basalt emplacement and dyke and sill intrusions may, however, have continued for millions of years into the Early Jurassic, with a late phase of CAMP magmatism dated as of Early–Middle Pliensbachian age by $^{40}Ar/^{39}Ar$ (Baksi and Archibald, 1997; Deckart et al., 1997; Marzoli et al., 1999; Hames et al., 2000; Knight et al., 2004; Marzoli et al., 2004; Beutel et al., 2005; Verati et al., 2007; Nomade et al., 2007; Jourdan et al., 2009; Marzoli et al., 2011).

Sinemurian and Pliensbachian seawater $^{87}Sr/^{86}Sr$ ratios are often considered to show a relatively constant decline towards the Early Toarcian minimum (with values down to ~0.70705), at which point relatively enhanced continental silicate weathering in response to Early Toarcian Karoo-Ferrar volcanism induced a rapid reversal of this trend to renewed relatively elevated seawater $^{87}Sr/^{86}Sr$ values (Cohen and Coe, 2007). However, this supposed constant rate of decline in seawater $^{87}Sr/^{86}Sr$ may be an artefact of the assumption of equal duration ammonite (sub-)zones. Conversion of the Pliensbachian seawater $^{87}Sr/^{86}Sr$ record of Jones et al. (1994) and Jenkyns et al. (2002) to the Pliensbachian astrochronological time scale proposed here shows 4 distinct phases of enhanced decline in seawater $^{87}Sr/^{86}Sr$ superimposed on the Early Jurassic long-term fall in values, with a potential periodicity of ~2.4 Myr (Figure 8). The veracity of the observed changes in this trend relies on the accuracy of the positioning of the base of individual (sub)zones in both the outcrops and especially the Mochras core, and their precision as time markers. Although ammonite stratigraphy in cores might generally be less precise compared to that in outcrops, where fossil occurrences can be traced laterally, along geographically extensive bedding-planes, the precision of the assigned bases of (sub)zones in the Mochras core is relatively good (Table 1; Supplementary Figure 7) and was further refined by the identification and correlation of recognized foraminiferal zones (Copestake and Johnson, 2013).

Phases of enhanced decline in seawater $^{87}Sr/^{86}Sr$ may reflect periodic, long-term (>Myr) Milankovitch-forced, decreases in global continental weathering rates, with a diminished flux of radiogenic Sr. Interestingly, the onset of the Pliensbachian Stage is also marked by a plateau in seawater $^{87}Sr/^{86}Sr$ ratios, with stable values for ~2 Myr, closely resembling the pattern in the base Jurassic Hettangian Stage during the major phase of CAMP emplacement (Figure 8). This plateau in $^{87}Sr/^{86}Sr$ temporally coincides with a late phase of CAMP magmatism, with surface flood-basalt and subsurface sill emplacement in the eastern USA, Brazil and Guinea (Figure 8; Deckart et al., 1997; Marzoli et al., 1999; Nomade et al., 2007). The onset and duration of this plateau in $^{87}Sr/^{86}Sr$ also directly coincides with the earliest Pliensbachian (*jamesoni* zone) negative CIE, similar in magnitude (~2–4‰) and duration to the earliest Jurassic (Hettangian) long-term 'main' negative CIE (Figure 8; Hesselbo et al., 2002; Korte et al., 2009; Ruhl et al., 2010; Bartolini et al. 2012). The observed Early Pliensbachian plateau in $^{87}Sr/^{86}Sr$ ratios may, therefore, reflect a second Early Jurassic phase of CAMP-induced climatic and carbon-cycle perturbation that, as inferred for the Hettangian, also led to increased global weathering and an enhanced radiogenic Sr flux from the continents to the oceans. The inference of the Early Pliensbachian plateau in $^{87}Sr/^{86}Sr$ ratios depends on (1) the correct biostratigraphical correlation between the $^{87}Sr/^{86}Sr$ record, as measured in outcrops, and the Mochras core-based Early Pliensbachian astrochronology and (2) the correctness of the interpreted unequal duration of Pliensbachian zones, specifically the Early Pliensbachian (*jamesoni*) (sub)zones. If all the above is correct, then one may

conclude that subsequent phases of CAMP volcanism led to elevated atmospheric pCO_2 and increased global continental (silicate) weathering rates that balanced the dominant long-term unradiogenic marine hydrothermal/basalt weathering Sr flux and resulted in the observed (Hettangian and Early Pliensbachian) ~2 Myr plateaus in the Early Jurassic $^{87}Sr/^{86}Sr$ record.

[6] CONCLUSIONS

Periodic alternations in lithology and geochemical palaeoenvironmental proxies through the expanded and biostratigraphically complete Pliensbachian of the Mochras core (Llanbedr/ Mochras Farm borehole, Wales, UK) reflect Milankovitch forcing, predominantly at precession and short- and long-eccentricity periodicities. The duration of Pliensbachian ammonite zones is cyclostratigraphically constrained at ~2.7 Myr (*jamesoni*), ~1.8 Myr (*ibex*), ~0.4 Myr (*davoei*), ~2.4 Myr (*margaritatus*) and ~1.4 Myr (*spinatum*), with a combined duration of ~8.7 Myr for the complete Pliensbachian Stage. These figures, combined with radiometric and astrochronological constraints on the age of the base of the Toarcian, suggest a Sinemurian–Pliensbachian boundary age of 192.5 ± 0.4 Ma.

Calibration of the floating astronomical time scale for the Pliensbachian to the 405 Kyr eccentricity solution (La2010d) gives absolute ages for the Pliensbachian ammonite biozone boundaries and the base Pliensbachian (*jamesoni* zone) global exogenic carbon cycle perturbation. The negative excursion in $\delta^{13}C$ in the base Pliensbachian has a 2–4‰ amplitude and an astrochronologically defined duration of ~2 Myr. The Late Pliensbachian (upper *margaritatus* zone) global positive excursion in $\delta^{13}C$, which coincides with a seawater cool phase in the European realm as revealed by $\delta^{18}O$ from macrofossil calcite, has a duration of ~0.6 Myr.

Calibration of the Pliensbachian $^{87}Sr/^{86}Sr$ record to the obtained astrochronological age model suggests modulation with a ~2.4 Myr periodicity of the Pliensbachian long-term decreasing trend to less radiogenic values. The Pliensbachian $^{87}Sr/^{86}Sr$ record also shows a stable plateau in the Early Pliensbachian *jamesoni* zone, coinciding with the observed $\delta^{13}C$ negative shift of 2–4‰, and possibly reflecting elevated continental weathering, with a relatively increased flux of radiogenic $^{87}Sr/^{86}Sr$ to the global oceans, in response to a late phase of enhanced global continental (silicate) weathering induced by CAMP volcanism.

ACKNOWLEDGEMENTS

We acknowledge funding for this study from Shell International Exploration & Production B.V., the International Continental Drilling Programme, and the Natural Environment Research Council (NE/G01700X/1). CVU acknowledges funding from Leopoldina, German National Academy of Sciences (grant no. LPDS 2014-08). We thank the British Geological Survey (BGS) for enabling access to the Mochras core and Charles J.B. Gowing (BGS) for supplying hand-held XRF equipment and assistance with analyses. We also thank Steve Wyatt (Oxford) and Mabs Gilmour (Open University) for help with Rock-Eval and $\delta^{13}C$ analyses. We are further grateful for the constructive reviews by Wolfgang Ruebsam, Blair Schoene and one anonymous reviewer, and the editorial guidance by Martin Frank. JBR publishes with the approval of the Executive Director, British Geological Survey (NERC).

FIGURE CAPTIONS

FIGURE 1 Early Jurassic palaeogeography showing the Mochras (Cardigan Bay Basin) and Staithes (Cleveland Basin) localities (red stars) at the northwestern extremity

of the Tethys Ocean. The figure is modified after Dera et al. (2011) and Korte et al. (2015).

FIGURE 2 The relative thickness of the Lower Jurassic stages in the Mochras core and outcrops and boreholes in the UK, France and Portugal (Ivimey-Cook, 1971; Cope et al., 1980; Whittaker and Green, 1983; Lorenz and Gely, 1994; Ainsworth and Riley, 2010; Brigaud et al., 2014; Mattioli et al., 2013; and references therein). The 'T', 'HS' and 'PL' numbers refer to the stratigraphical columns in Cope et al. (1980).

FIGURE 3 Early Pliensbachian (*jamesoni* zone) lithology and XRF-derived geochemical data (calcium, titanium, iron, rubidium) showing sub-metre scale fluctuations. Calcium concentrations are superimposed on stacked core photographs showing a clear association with lithology/rock-colour. Four to five carbonate beds are grouped into bundles (E^{-1}) and super-bundles (E^{-2}), hypothetically representing short (~100 Kyr) and long (~405 Kyr) eccentricity. High values for Ti, Fe and Rb correlate closely with periodically low concentrations of Ca, suggesting carbonate dilution of other sedimentary components.

FIGURE 4 XRF-derived calcium and titanium record spanning the entire Pliensbachian Stage (from the Late Sinemurian *raricostatum* zone into the Early Toarcian *tenuicostatum* zone). Mochras core biostratigraphy following Ivimey-Cook (1971), Page (2003), and Copestake and Johnson (2013). The palaeomagnetic field directions from numerous outcrop studies are correlated to the Mochras core biostratigraphical record following the Geological Time Scale (GTS) 2012 (Gradstein et al., 2012). Ca content, superimposed on the stacked core photograph record, shows short-, intermediate- and long-periodicity fluctuations, with (A) the complete core, (B) part of the Late Sinemurian *raricostatum* and complete Early Pliensbachian *jamesoni* ammonite zones, (C) the Pliensbachian *ibex* and *davoei* ammonite zones and (D) the Upper Pliensbachian *margaritatus* and *spinatum* ammonite zones. The short- and intermediate-periodicity band-pass filters reflect dominant spectral peaks in the depth-domain (Supplementary Figure 2; see also section 5.3), suggesting a combined duration of ~8.7 Myr for the complete Pliensbachian Stage (see Supplementary Figure 4). Grey arrows show intervals with possibly dominant obliquity forcing.

FIGURE 5 Multi-taper (MTM; 3π) spectral and wavelet analyses of the XRF elemental (Fe) time series obtained using the Astrochron toolkit (R (3.1.2) Package for astrochronology, version 0.3.1; Meyers, 2014), with robust red noise models (Mann and Lees, 1996). The elemental Fe record was first re-sampled to uniform sample spacing using linear interpolation. Initial spectral analysis was performed with AnalySeries on a detrended data-series (with low band-pass filtering to remove >150 m periodicities). Dominant spectral components (Supplementary Figures 2, 3) were filtered from the data series and compared to the visually defined precession and short- and long-eccentricity periodicities (Figure 4). The elemental Fe record in the depth domain was subsequently converted to the time domain following the observed 405 Kyr eccentricity cycles. The multi-taper (MTM; 3π) spectral and wavelet analyses of the obtained elemental (Fe) time series show dominant and significant peaks at precession (~21 and ~26 Kyr), obliquity (~41 Kyr), short-period eccentricity (~100 and ~134 Kyr), long-period eccentricity (~405 Kyr) and also long-term periodicity (~640 and 2500 Kyr).

FIGURE 6 Calibration of the obtained Pliensbachian 405-Kyr eccentricity series to the astronomical solution (La2010d) of Laskar et al. (2011) allows for 3 different options

(A, B and C) due to the ~250 Kyr uncertainty in U-Pb radiometric dating of the base *falciferum* zone in the Pucara Basin in Peru and the ~200 Kyr uncertainty in the astrochronologically estimated duration of the base Toarcian *polymorphum* (*tenuicostatum*) zone in the Lusitanian Basin, Portugal (see also section 7.2). Radiometric and astrochronological constraints on the age of the base-Hettangian (Triassic–Jurassic) and base-Sinemurian Stage boundaries and the duration of the Hettangian Stage and the *polymorphum* zone are from Kent and Olsen (2008), Schaltegger et al. (2008), Suan et al. (2008), Ruhl et al. (2010), Schoene et al. (2010), Guex et al. (2012), Blackburn et al. (2013), Huang and Hesselbo (2014), Hüsing et al. (2014) and Sell et al. (2014). Orange bars present the reported radiometric uncertainty. The Hettangian palaeomagnetic record is from Kent and Olsen (2008) and Hüsing et al. (2014). The Pliensbachian palaeomagnetic record is from the Geological Time Scale (GTS) 2012 (Gradstein et al., 2012).

FIGURE 7 The Pliensbachian $\delta^{13}C$ record of marine calcite and wood from UK outcrops (Jenkyns et al., 2002; Korte and Hesselbo, 2011) and $\delta^{13}C$ of bulk organic matter ($\delta^{13}C_{TOC}$) from Staithes (this study; Yorkshire, UK (locality described in Korte and Hesselbo, 2011)), calibrated to the Pliensbachian floating astronomical time scale, using zone boundaries as tie-points and linear-interpolation within a zone.

FIGURE 8 The Pliensbachian seawater $^{87}Sr/^{86}Sr$ record calibrated against the newly derived floating astrochronological time scale, using subzone boundaries in outcrops (that yielded $^{87}Sr/^{86}Sr$ data) and the Mochras core as tie-points, and linear interpolation within subzones. The time-calibrated $^{87}Sr/^{86}Sr$ record shows periodically enhanced decline (grey arrows) superimposed on a long-term decrease from ~0.70745 to ~0.70710. The base of the Pliensbachian is, furthermore, marked by a plateau in $^{87}Sr/^{86}Sr$ (blue arrows), coinciding with a global carbon-cycle perturbation and recurrent Central Atlantic Magmatic Province (CAMP) volcanism. Early Jurassic $^{87}Sr/^{86}Sr$ values are from Jones et al. (1994b) and Jenkyns et al. (2002) (data were normalized to a value of the NBS987 standard of 0.710250, with $24*10^{-6}$ added to the published data of Jones et al. (1994b), which was normalized to a different standard). The Pliensbachian $\delta^{13}C$ record is from Jenkyns et al. (2002) and Korte and Hesselbo (2011). Upper Triassic/Lower Jurassic radiometric dating of CAMP magmatism comes from Baksi and Archibald (1997), Deckart et al. (1997), Marzoli et al. (1999), Hames et al. (2000), Marzoli et al. (2004), Knight et al. (2004), Beutel et al. (2005), Verati et al. (2007), Nomade et al. (2007), Jourdan et al. (2009), Marzoli et al. (2011) and Blackburn et al. (2013). The dark grey area in the upper graph shows the cumulative probability of CAMP magmatism through time, following uncertainties on U-Pb and the recalculated $^{40}Ar/^{39}Ar$ radiometric dates of individual basalt formations.

TABLE 1 Absolute age, uncertainty and duration estimates for the (base of) the Early Jurassic stages (Hettangian, Sinumurian, Pliensbachian and Toarcian) and the Hettangian and Pliensbachian zones. Basal-age and durations based on Kent and Olsen (2008), Schaltegger et al. (2008), Suan et al. (2008), Ruhl et al. (2010), Schoene et al. (2010), Guex et al. (2012), Blackburn et al. (2013), Boulila et al., 2014; Huang and Hesselbo (2014), Hüsing et al. (2014), Ruebsam et al., 2014 and Sell et al. (2014).

REFERENCES

Allègre, C.J., Louvat, P., Gaillardet, J., Meynadier, L., Rad, S., Capmas, F., The fundamental role of island arc weathering in the oceanic Sr isotope budget. Earth and Planetary Science Letters 292, p. 51–56 (2010).

Al-Suwaidi, A.H., Hesselbo, S.P., Damborenea, S.E., Mancenido, M.O., Jenkyns, H.C., Riccardi, A.C., Angelozzi, G.N., Baudin, F., The Toarcian Oceanic Anoxic Event (Early Jurassic) in the Neuquén Basin, Argentina: A reassessment of age and carbon-isotope stratigraphy. The Journal of Geology 124, p. 171–193 (2016).

Armendariz, M., Rosales, I., Badenas, B., Aurell, M., Garcia-Ramos, J.C., Pinuela, L., High-resolution chemostratigraphic records from the Lower Pliensbachian belemnites: Palaeoclimatic perturbations, organic facies and water mass exchange (Asturian basin, northern Spain). Palaeogeography, Palaeoclimatology, Palaeoecology 333-334, p. 178–191 (2012).

Armendariz, M., Rosales, I., Badenas, B., Pinuela, L., Aurell, M., Garcia-Ramos, J.C., An approach to estimate Lower Jurassic seawater oxygen-isotope composition using $\delta^{18}O$ and Mg/Ca ratios of belemnite calcites (Early Pliensbachian, northern Spain). Terra Nova 25, p. 439–445 (2013).

Baksi, A.K., Archibald, D.A., Mesozoic igneous activity in the Maranhao province, northern Brazil: $^{40}Ar/^{39}Ar$ evidence for separate episodes of basaltic magmatism. Earth and Planetary Science Letters 151, p. 139–153 (1997).

Bartolini, A., Guex, J., Spangenberg, J.E., Schoene, B., Taylor, D.G., Schaltegger, U., Atudorei, V., Disentangling the Hettangian carbon isotope record: Implications for the aftermath of the end-Triassic mass extinction. Geochemistry, Geophysics, Geosystems 13, no. 1 (2012).

Beutel, E.K., Nomade, S., Fronabarger, A.K., Renne, P.R., Pangea's complex breakup: A new rapidly changing stress field model. Earth and Planetary Science Letters 236, p. 471–485 (2005).

Blackburn, T.J., Olsen, P.E., Bowring, S.A., McLean, N.M., Kent, D.V., Puffer, J., McHone, G., Rasbury, E.T., Et-Touhami, M., Zircon U-Pb geochronology links the end-Triassic extinction with the Central Atlantic Magmatic Province. Science 340, p. 941–945 (2013).

Bonis, N.R., Kürschner, W.M., Vegetation history, diversity patterns, and climate change across the Triassic/Jurassic boundary. Paleobiology 38, p. 240–264 (2012).

Boulila, S., Galbrun, B., Huret, E., Hinnov, L.A., Rouget, I., Gardin, S., Huang, C., and Bartolini, A., Astronomical calibration of the Toarcian Stage: implications for sequence stratigraphy and duration of the Early Toarcian OAE, Earth and Planetary Science Letters 386, p. 98-111 (2014).

Brazier, J.-M., Suan, G., Tacail, T., Simon, L., Martin, J.E., Mattioli, E., Balter, V., Calcium isotopic evidence for dramatic increase of continental weathering during the Toarcian oceanic anoxic event (Early Jurassic). Earth and Planetary Science Letters 411, p. 164–176 (2015).

Burgess, S.D., Bowring, S.A., Fleming, T.H., Elliot, D.H., High-precision geochronology links the Ferrar large igneous province with Early Jurassic ocean anoxia and biotic crisis. Earth and Planetary Science Letters 415, p. 90–99 (2015).

Burke, W.H., Denison, R.E., Hetherington, E.A., Koepnick, R.B., Nelson, H.F., Otto, J.B., Variation of seawater $^{87}Sr/^{86}Sr$ throughout Phanerozoic time. Geology 10, p. 516–519 (1982).

Clemence, M.-E., Bartolini, A., Gardin, S., Paris, G., Beaumont, V., Page, K.N., Early Hettangian benthic-planktonic coupling at Doniford (SW England): Palaeoenvironmental implications for the aftermath of the end-Triassic crisis. Palaeogeography, Palaeoclimatology, Palaeoecology 295, p. 102–115 (2010).

Close, R.A., Friedman, M., Lloyd, G.T., Benson, R.B.J., Evidence for a Mid-Jurassic Adaptive Radiation in Mammals. Current Biology 25, p. 1–6 (2015).

Cohen, A.S., Coe, A.L., Harding, S.M., Schwark, L., Osmium isotope evidence for the regulation of atmospheric CO_2 by continental weathering. Geology 32, n. 2, p. 157–160 (2004).

Cohen, A.S., Coe, A.L., The impact of the Central Atlantic Magmatic Province on climate and on the Sr- and Os-isotope evolution of seawater. Palaeogeography, Palaeoclimatology, Palaeoecology 244, p. 374–390 (2007).

Copestake, P., Johnson, B., Lower Jurassic foraminifera from the Llanbedr (Mochras Farm) borehole, North Wales, UK. Monograph of the Palaeontographical Society, London 167, p. 1–403 (2014).

874 Crowley, J.W., Katz, R.F., Huybers, P., Langmuir, C.H., Park, S.-H., Glacial cycles drive
875 variations in the production of oceanic crust. Science 347, p. 1237–1240 (2015).
876 Dal Corso, J., Marzoli, A., Tateo, F., Jenkyns, H.C., Bertrand, H., Youbi, N., Mahmoudi, A.,
877 Font, E., Buratti, N., Cirilli, S., The dawn of CAMP volcanism and its bearing on the end-
878 Triassic carbon cycle disruption. Journal of the Geological Society, London 171, p. 153–
879 164 (2014).
880 Deckart, K., Feraud, G., Bertrand, H., Age of Jurassic continental tholeiites of French Guyana,
881 Surinam and Guinea: Implications for the initial opening of the Central Atlantic Ocean.
882 Earth and Planetary Science Letters 150, p. 205–220 (1997).
883 Deenen, M.H.L., Krijgsman, W., Ruhl, M., The quest for chron E23r at Partridge Island, Bay of
884 Fundy, Canada: CAMP emplacement postdates the end-Triassic extinction event at the
885 North American craton. Canadian Journal of Earth Science 48, p. 1282–1291 (2011).
886 Deenen, M.H.L., Ruhl, M., Bonis, N.R., Krijgsman, W., Kuerschner, W.M., Reitsma, M., van
887 Bergen, M.J., A new chronology for the end-Triassic mass extinction. Earth and Planetary
888 Science Letters 291, p. 113–125 (2010).
889 Dera, G., Neige, P., Dommergues, J.-L., Brayard, A., Ammonite paleobiogeography during the
890 Pliensbachian–Toarcian crisis (Early Jurassic) reflecting paleoclimate, eustasy, and
891 extinctions. Global and Planetary Change 78, p. 92–105 (2011).
892 Dobson M.R., Whittington, R.J., The geology of Cardigan Bay, Proceedings of the Geologists'
893 Association 98, p. 331–353 (1987).
894 Elderfield, H., Strontium isotope stratigraphy, Palaeogeography, Palaeoclimatology,
895 Palaeoecology 57, p. 71–90 (1986).
896 Fernandes, S., Font, E., Neres, M., Martins, L., Youbi, N., Madeira, J., Marzoli, A., The Central
897 Atlantic Magmatic Province (CAMP) in Portugal, high eruption rate in one short-lived
898 volcanic pulse. Comunicacoes Geologicas 101, p. 1449–1453 (2014).
899 Fleet, A.J., Clayton, C.J., Jenkyns, H.C., Parkinson, D.N., Liassic source-rock deposition in
900 Western Europe. In: Brooks, J., Glennie, K. (Eds.), Petroleum Geology of North-west
901 Europe, 1, Graham and Trotman, p. 59–70 (1987).
902 Franceschi, M., Dal Corso, J., Posenato, R., Roghi, G., Masetti, D., Jenkyns, H.C., Early
903 Pliensbachian (Early Jurassic) C-isotope perturbation and the diffusion of the Lithiotis
904 Fauna: Insights from the western Tethys. Palaeogeography, Palaeoclimatology,
905 Palaeoecology 410, p. 255–263 (2014).
906 Gomez, J.J., Comas-Rengifo, M.J., Goy, A., Palaeoclimatic oscillations in the Pliensbachian
907 (Lower Jurassic) of the Asturian Basin (Northern Spain). Climate of the Past Discussions
908 11, p. 4039–4076 (2015).
909 Gradstein, F.M., Ogg, J.G., Schmitz, M.D., Ogg, G.M., The Geological Time Scale 2012, Volume
910 1 & 2, Elsevier, ISBN: 978-0-44-459390-0 & 978-0-44-459434-1 (2012).
911 Guex, J., Bartolini, A., Spangenberg, J., Vicente, J.-C., Schaltegger, U., Ammonoid multi-
912 extinction crises during the Late Pliensbachian–Toarcian and carbon cycle instabilities.
913 Solid Earth Discussions 4, p. 1205–1228 (2012).
914 Guex, J., Schoene, B., Bartolini, A., Spangenberg, J., Schaltegger, U., O'Dogherty, L., Taylor, D.,
915 Bucher, H., Atudorei, V., Geochronological constraints on post-extinction recovery of the
916 ammonoids and carbon cycle perturbations during the Early Jurassic. Palaeogeography,
917 Palaoeclimatology, Palaeoecology 346-347, p. 1–11 (2012).
918 Hallam, A., Origin of minor limestone-shale cycles: Climatically induced or diagenetic? Geology
919 14, p. 609–612 (1986).
920 Hallam, A., Estimates of the amount and rate of sea-level change across the Rhaetian-Hettangian
921 and Pliensbachian-Toarcian boundaries (latest Triassic to Early Jurassic). Journal of the
922 Geological Society 154, p. 773–779 (1997).
923 Hames, W.E., Renne, P.R., Ruppel, C., New evidence for geological instantaneous emplacement
924 of earliest Jurassic central Atlantic Magmatic Province basalts on the North American
925 margin. Geology 28, p. 859–862 (2000).
926 Hesselbo, S.P., Bjerrum, C.J., Hinnov, L.A., MacNiocaill, C., Miller, K.G., Riding, J.B., van de
927 Schootbrugge, B., and the Mochras Revisited Science Team, Mochras borehole revisited: a
928 new global standard for Early Jurassic earth history. Scientific Drilling 16, p. 81–91 (2013).

929 Hesselbo, S.P., Jenkyns, H.C., A comparison of the Hettangian to Bajocian successions of Dorset
930 and Yorkshire. From Taylor, P.D. (Ed.): Field Geology of the British Jurassic. Geological
931 Society, London, p. 105–150 (1995).
932 Hesselbo, S.P., Jenkyns, H.C., British Lower Jurassic sequence stratigraphy. In (de Graciansky,
933 P.C., Hardenbol, J., Jacquin, T., Farley, M. & Vail, P.R. (Eds.) Mesozoic–Cenozoic
934 Sequence Stratigraphy of European Basins. Society for Sedimentary Geology (SEPM),
935 Special Publication, 60, p. 561–581 (1998).
936 Hesselbo, S.P., Meister, C., Grocke, D.R., A potential global stratotype for the Sinemurian-
937 Pliensbachian boundary (Lower Jurassic), Robin Hood's Bay, UK: ammonite faunas and
938 isotope stratigraphy. Geological Magazine 137, p. 601–607 (2000).
939 Hesselbo, S.P., Robinson, S.A., Surlyk, F., Piasecki, S., Terrestrial and marine extinction at the
940 Triassic-Jurassic boundary synchronized with major carbon-cycle perturbation: A link to
941 initiation of massive volcanism? Geology 30, p. 251–254 (2002).
942 Hesselbo, S.P., Robinson, S.A., Surlyk, F., Sea-level change and facies development across
943 potential Triassic-Jurassic boundary horizons, SW Britain. Journal of the Geological
944 Society, London 161, p. 365–379 (2004).
945 Hesselbo, S.P., Sequence stratigraphy and inferred relative sea-level change from the onshore
946 British Jurassic. Proceedings of the Geologists' Association 119, p. 19–34 (2008).
947 Hilgen, F.J., Hinnov, L.A., Abdul Aziz, H., Abels, H.A., Batenburg, S., Bosmans, J.H.C., de Boer,
948 B., Hüsing, S.K., Kuiper, K.F., Lourens, L.J., Rivera, T., Tuenter, E., Van de Wal, R.S.W.,
949 Wotzlaw, J.-F., Zeeden, C., Stratigraphic continuity and fragmentary sedimentation: the
950 success of cyclostratigraphy as part of integrated stratigraphy. From: Smith, D.G., Bailey,
951 R.J., Burgess, P.M., Fraser, A.J. (eds): Strata and Time: Probing the gaps in our
952 understanding. Geological Society, London, Special Publication 404, p. 157–197 (2014).
953 Hori, R., Lower Jurassic radiolarian zones of SW Japan. Transactions and Proceedings of the
954 Palaeontological Society of Japan, N.S. 159, p. 562–586 (1990).
955 Hori, R., Radiolarian biostratigraphy at the Triassic–Jurassic period boundary in bedded cherts
956 from the Inuyama area, Central Japan. Journal of Geosciences Osaka City University 35, p.
957 53–65 (1992).
958 Hori, S.R., The Toarcian radiolarian event in bedded cherts from southwestern Japan. Marine
959 Micropaleontology 30, p. 159–169 (1997).
960 Huang, C., Hesselbo, S.P., Pacing of the Toarcian Oceanic Anoxic Event (Early Jurassic) from
961 astronomical correlation of marine sections. Gondwana Research 25, p. 1348–1356 (2014).
962 Hüsing, S.K., Beniest, A., Van der Boon, A., Abels, H.A., Deenen, M.H.L., Ruhl, M., Krijgsman,
963 W., Astronomically-calibrated magnetostratigraphy of the Lower Jurassic marine
964 successions at St Audrie's Bay and East Quantoxhead (Hettangian-Sinemurian; Somerset,
965 UK). Palaeogeography, Palaoeclimatology, Palaeoecology 403, p. 43–56 (2014).
966 Ikeda, M., Hori, R.S., Effects of Karoo–Ferrar volcanism and astronomical cycles on the
967 Toarcian Oceanic Anoxic Events (Early Jurassic). Palaeogeography, Palaeoclimatology,
968 Palaeoecology 410, p. 134–142 (2014).
969 Ikeda, M., Tada, R., A 70 million year astronomical time scale for the deep-sea bedded chert
970 sequence (Inuyama, Japan): Implications for Triassic–Jurassic geochronology. Earth and
971 Planetary Science Letters 399, p. 30–43 (2014).
972 Ivimey-Cook, H.C., Stratigraphical Palaeontology of the Lower Jurassic of the Llanbedr
973 (Mochras Farm) Borehole. In: Woodland, A.W. (Ed). The Llanbedr (Mochras Farm)
974 Borehole. Institute of Geological Sciences Report No. 71/18, p. 87–92 (1971).
975 Jenkyns, H.C., Clayton, C.J., Black shales and carbon isotopes in pelagic sediments from the
976 Tethyan Lower Jurassic. Sedimentology 33, p. 87–106 (1986).
977 Jenkyns, H.C., Evidenc for rapid climate change in the Mesozoic–Palaeogene greenhouse world.
978 Philosophical Transactions of the Royal Society London A 361, p. 1885-1916 (2003).
979 Jenkyns, H.C., Geochemistry of oceanic anoxic events. Geochemistry, Geophysics, Geosystems
980 11, Q03004, DOI: 10.1029/2009GC002788 (2010).
981 Jenkyns, H.C., Jones, C.E., Grocke, D.R., Hesselbo, S.P., Parkinson, D.N., Chemostratigraphic
982 of the Jurassic System: applications, limitations and implications for palaeoceanography.
983 Journal of the Geological Society 159, p. 351–378 (2002).

Jenkyns, H.C., Weedon, G.P., Chemostratigraphic ($CaCO_3$, TOC, $\delta^{13}C_{org}$) of Sinemurian (Lower Jurassic) black shales from the Wessex Basin, Dorset and palaeoenvironmental implications. Newsletters on Stratigraphy 46, p. 1–21 (2013).

Jones, C.E., Jenkyns, H.C., Coe, A.L., Hesselbo, S.P., Strontium isotopic variations in Jurassic and Cretaceous seawater. Geochimica et Cosmochimica Acta 58, p. 3061–3074 (1994 a).

Jones, C.E., Jenkyns, H.C., Hesselbo, S.P., Strontium isotopes in Early Jurassic seawater. Geochimica et Cosmochimica Acta 58, p. 1285–1301 (1994 b).

Jones, C.E., Jenkyns, H.C., Seawater strontium isotopes, oceanic anoxic events, and seafloor hydrothermal activity in the Jurassic and Cretaceous. American Journal of Science 301, p. 112–149 (2001).

Jourdan, F., Marzoli, A., Bertrand, H., Cirilli, S., Tanner, L.H., Kontak, D.J., McHone, G., Renne, P.R., Bellieni, G., $^{40}Ar/^{39}Ar$ age of CAMP in North America: Implications for the Triassic-Jurassic boundary and the ^{40}K decay constant bias. Lithos 110, p. 167–180 (2009).

Kemp, D.B., Coe, A.L., Cohen, A.S., Weedon, G.P., Astronomical forcing and chronology of the Early Toarcian (Early Jurassic) oceanic anoxic event in Yorkshire, UK. Paleoceanography 26, PA4210 (2011).

Kent, D.V., Olsen, P.E., Early Jurassic magnetostratigraphy and paleolatitudes from the Hartford continental rift basin (eastern North America): Testing for polarity bias and abrupt polar wander in association with the Central Atlantic Magmatic Province. Journal of Geophysical Research 113, B06105 (2008).

Knight, K.B., Nomade, S., Renne, P.R., Marzoli, A., Bertrand, H., Youbi, N., The Central Atlantic Magmatic Province at the Triassic-Jurassic boundary: paleomagnetic and $^{40}Ar/^{39}Ar$ evidence from Morocco for brief, episodic volcanism. Earth and Planetary Science Letters 228, p. 143–160 (2004).

Korte, C., Hesselbo, S.P., Jenkyns, H.C., Rickaby, R.E.M., Spotl, C., Palaeoenvironmental significance of carbon- and oxygen-isotope stratigraphy of marine Triassic Jurassic boundary sections in SW Britain. Journal of the Geological Society 166, p. 431–445 (2009).

Korte, C., Hesselbo, S.P., Shallow marine carbon and oxygen isotopic and elemental records indicate icehouse-greenhouse cycles during the Early Jurassic. Paleoceanography 26, PA4219 (2011).

Korte, C., Hesselbo, S.P., Ullmann, C.V., Dietl, G., Ruhl, M., Schweigert, G., Thibault, T., Jurassic climate mode governed by ocean gateway. Nature Communications 6, p. 10015 (2015).

Krabbenhöft, A., Eisenhauer, A., Böhm, F., Vollstaedt, H., Fietzke, J., Liebetrau, V., Augustin, N., Peucker-Ehrenbrink, B., Muller, M.N., Horn, C., Hansen, B.T., Nolte, N., Wallmann, K., Constraining the marine strontium budget with natural strontium isotope fractionations ($^{87}Sr/^{86}Sr^*$, $\delta^{88/86}Sr$) of carbonates, hydrothermal solutions and rivers. Geochimica et Cosmochimica Acta 74, p. 4097–4109 (2010).

Krencker, F.-N., Bodin, S., Suan, G., Heimhofer, U., Kabiri, L., Immenhauser, A., Toarcian extreme warmth led to tropical cyclone intensification. Earth and Planetary Science Letters 425, p. 120–130 (2015).

Laskar, J., Fienga, A., Gastineau, M., Manche, H., La2010: a new orbital solution for the long-term motion of the Earth. Astronomy & Astrophysics 532, A89 (2011).

Laskar, J., Robutel, P., Joutel, F., Gastineau, M., Correia, A.C.M., Levrard, B., A long-term numerical solution for the insolation quantities of the Earth. Astronomy & Astrophysics 428, p. 261–285 (2004).Mann, M.E., Lees, J.M., Robust estimation of background noise and signal detection in climatic time series. Climatic Change 33, p. 409–445 (1996).

Marzoli, A., Bertrand, H., Knight, K.B., Cirilli, S., Buratti, N., Verati, C., Nomade, S., Renne, P.R., Youbi, N., Martini, R., Allenbach, K., Neuwerth, R., Rapaille, C., Zaninetti, L., Bellieni, G., Synchrony of the Central Atlantic Magmatic Province and the Triassic-Jurassic boundary climatic and biotic crisis. Geology 32, p. 973–976 (2004).

Marzoli, A., Jourdan, F., Puffer, J.H., Cuppone, T., Tanner, L.H., Weems, R.E., Bertrand, H., Cirilli, S., Bellieni, G., De Min, A., Timing and duration of the Central Atlantic Magmatic Province in the Newark and Culpeper basins, eastern U.S.A. Lithos 122, p. 175–188 (2011).

Marzoli, A., Renne, P.R., Piccirillo, E.M., Ernesto, M., Bellieni, G., De Min, A., Extensive 200-million-year-old continental flood basalts of the Central Atlantic Magmatic Province. Science 284, p. 616 (1999).

McArthur, J.M., Donovan, D.T., Thirlwall, M.F., Fouke, B.W., Mattey, D., Strontium isotope profile of the Early Toarcian (Jurassic) oceanic anoxic event, the duration of ammonite biozones and belemnite palaeotemperatures. Earth and Planetary Science Letters 179, p. 269–285 (2000).

McArthur, J.M., Steuber, T., Page, K.N., Landman, N.H., Sr-isotope stratigraphy: Assigning time in the Campanian, Pliensbachian, Toarcian and Valanginian. The Journal of Geology 124, p. 000–000, 2016 (2016).

McElwain, J.C., Beerling, D.J., Woodward, F.I., Fossil plants and global warming at the Triassic-Jurassic boundary. Science 285, p. 1386 (1999).

Meister, C., Aberhan, M., Blau, J., Dommergues, J.-L., Feist-Burkhardt, S., Hailwood, E.A., Hart, M., Hesselbo, S.P., Hounslow, M.W., Hylton, M., Morton, N., Page, K., Price, G., the Global Boundary Stratotype Section and Point (GSSP) for the base of the Pliensbachian Stage (Lower Jurassic), Wine Haven, Yorkshire, UK. Episodes 20, 93-106 (2006).

Meyers, S.R., Astrochron: An R Package for Astrochronology (Version 0.3.1). http://cran.r-project.org/package=astrochron) (2014).

Morettini, E., Santantonio, M., Bartolini, A., Cecca, F., Baumgartner, P.O., Hunziker, J.C., Carbon isotope stratigraphy and carbonate production during the Early-Middle Jurassic: examples from the Umbria-Marche-Sabine Apennines (central Italy). Palaeogeography, Palaeoclimatology, Palaeoecology 184, p. 251–273 (2002).

Nomade, S., Knight, K.B., Beutel, E., Renne, P.R., Verati, C., Feraud, G., Marzoli, A., Youbi, N., Bertrand, H., Chronology of the Central Atlantic Magmatic Province: Implications for the Central Atlantic rifting process and the Triassic–Jurassic biotic crisis. Palaeogeography, Palaeoclimatology, Palaeoecology 244, p. 326–344 (2007).

Olsen, P.E., Stratigraphic record of the Early Mesozoic breakup of Pangea in the Laurasia-Gondwana rift system. Annual Review of Earth and Planetary Sciences 25, p. 337–401 (1997).

Olsen, P.E., Kent, D.V., Et-Touhami, M., Puffer, J., Cyclo-, magneto, and bio-stratigraphic constraints on the duration of the CAMP event and its relationship to the Triassic-Jurassic boundary. From: The Central Atlantic Magmatic Province: Insights from fragments of Pangea. Geophysical Monograph 136, American Geophysical Union (2003).Page, K.N., Bello, J., Dolores Lardies, M., Melendez, G., Ramajo, J., Ziani, H., The stratigraphy of the upper Bathonian to middle Oxfordian succession of the aragonese branch of the Cordillera Iberica (Spain) and its European context. Rivista Italiana do Paleontologia e Stratigrafia 110, p. 191–200 (2004).

Page, K.N., The Lower Jurassic of Europe; its subdivision and correlation. Geological Survey of Denmark and Greenland Bulletin 1, p. 23–59 (2003).

Paillard, D., Labeyrie, L., Yiou, P., Macintosh program performs time-series analysis, Eos, Transactions of the American Geophysical Union 77: 379 (1996).

Pálfy, J., Smith, P.L., Synchrony between Early Jurassic extinction, oceanic anoxic event, and the Karoo-Ferrar flood basalt volcanism. Geology 28, n. 8, p. 747–750 (2000).

Percival, L.M.E., Witt, M.L.I., Mather, T.A., Hermoso, M., Jenkyns, H.C., Hesselbo, S.P., Al-Suwaidi, A.H., Storm, M.S., Xu, W., Ruhl, M., Globally enhanced mercury deposition during the end-Pliensbachian extinction and Toarcian OAE: A link to the Karoo–Ferrar Large Igneous Province. Earth and Planetary Science Letters 428, p. 267–280 (2015).

Porter S.J., Selby, D., Suzuki, K., Grocke, D., opening of a trans-Pangaean marine corridor during the Early Jurassic: Insights from osmium isotopes across the Sinemurian-Pliensbachian GSSP, Robin Hood's Bay, UK. Palaeogeography, Palaeoclimatology, Palaeoecology 375, p. 50–58 (2013).

Riding, J.B., Leng, M.J., Kender, S., Hesselbo, S.P., Feist-Burkhardt, S., Isotopic and palynological evidence for a new Early Jurassic environmental perturbation. Palaeogeography, Palaeoclimatology, Palaeoecology 374, p. 16-27 (2013).

1093 Ruebsam, W., Munzberger, P., Schwark, L., Chronology of the Early Toarcian environmental
1094 crisis in the Lorraine Sub-Basin (NE Paris Basin). Earth and Planetary Science Letters 404,
1095 p. 273–282 (2014).
1096 Ruebsam, W., Munzberger, P., Schwark, L., Reply to the comment by Boulila and Hinnov
1097 towards "Chronology of the Early Toarcian environmental crisis in the Lorraine Sub-Basin
1098 (NE Paris Basin). Earth and Planetary Science Letters 404, p. 273–282 (2014)". Earth and
1099 Planetary Science Letters 416, 147–150 (2015).
1100 Ruhl, M., Bonis, N.R., Reichart, G.-J., Sinninghe Damste, J.S., Kürschner, W.M., Atmospheric
1101 carbon injection linked to End-Triassic mass extinction. Science 333, p. 430 (2011).
1102 Ruhl, M., Deenen, M.H.L., Abels, H.A., Bonis, N.R., Krijgsman, W., Kürschner, W.M.,
1103 Astronomical constraints on the duration of the Early Jurassic Hettangian Stage and
1104 recovery rates following the end-Triassic mass extinction (St Audrie's Bay/East
1105 Quantoxhead, UK). Earth and Planetary Science Letters 295, p. 262–276 (2010).
1106 Ruhl, M., Kürschner, W.M., Multiple phases of carbon cycle disturbance from large igneous
1107 province formation at the Triassic-Jurassic transition. Geology 39, p. 431–434 (2011).
1108 Schaller, M. F., Wright, J.D., Kent, D.V., Atmospheric pCO2 perturbations associated with the
1109 Central Atlantic Magmatic Province. Science 331, p. 1404 (2011).
1110 Schaltegger, U., Guex, J., Bartolini, A., Schoene, B., Ovtcharova, M., Precise U-Pb age
1111 constraints for end-Triassic mass extinction, its correlation to volcanism and Hettangian
1112 post-extinction recovery. Earth and Planetary Science Letters 267, p. 266–275 (2008).
1113 Schoene, B., Guex, J., Bartolini, A., Schaltegger, U., Blackburn, T.J., Correlating the end-Triassic
1114 mass extinction and flood basalt volcanism at the 100 ka level. Geology 38, p. 387–390
1115 (2010).
1116 Sell, B., Ovtcharova, M., Guex, J., Bartolini, A., Jourdan, F., Spangenberg, J.E., Vicente, J.-C.,
1117 Schaltegger, U., Evaluating the temporal link between the Karoo LIP and climatic-biologic
1118 events of the Toarcian Stage with high-precision U-Pb geochronology. Earth and
1119 Planetary Science Letters 408, p. 48–56 (2014).
1120 Sellwood, B.W., Regional environmental changes across a Lower Jurassic stage-boundary in
1121 Britain. Palaeontology 15, p. 125 (1972).
1122 Sellwood, B.W., The relation of trace fossils to small scale sedimentary cycles in the British Lias.
1123 From: crimes, I.P. and Harper, J.C., (eds): Trace Fossils. Seel House Press, Liverpool,
1124 Special Issue Geological Journal, p. 489–504 (1970).
1125 Silva, R.L., Duarte, L.V., Comas-Rengifo, M.J., Mendonca Filho, J.G., Azeredo, A.C., Update of
1126 the carbon and oxygen isotopic records of the Early–Late Pliensbachian (Early Jurassic,
1127 ~187 Ma): Insights from the organic-rich hemipelagic series of the Lusitanian Basin
1128 (Portugal). Chemical Geology 283, p. 177–184 (2011).
1129 Silva, R.L., Duarte, L.V., Organic matter production and preservation in the Lusitanian Basin
1130 (Portugal) and Pliensbachian climatic hot snaps. Global and Planetary Change 131, p. 24–
1131 34 (2015).
1132 Steinthorsdottir, M., Vajda, V., Early Jurassic (late Pliensbachian) CO_2 concentrations based on
1133 stomatal analysis of fossil conifer leaves from eastern Australia. Gondwana Research 27, p.
1134 932–939 (2013).
1135 Steuber, T., Veizer, J., Phanerozoic record of plate tectonic control of seawater chemistry and
1136 carbonate sedimentation. Geology 30, p. 1123–1126 (2002).
1137 Suan, G., Mattioli, E., Pittet, B., Lecuyer, C., Sucheras-Marx, B., Duarte, L.V., Philippe, M.,
1138 Reggiani, L., Martineau, F., Secular environmental precursors to Early Toarcian (Jurassic)
1139 extreme climate changes. Earth and Planetary Science Letters 290, p. 448–458 (2010).
1140 Suan, G., Nikitenko, B.L., Rogov, M.A., Baudin, F., Spangenberg, J.E., Knyazev, V.G., Glinskikh,
1141 L.A., Goryacheva, A.A., Adatte, T., Riding, J.B., Föllmi, K.B., Pittet, B., Mattioli, E.,
1142 Lecuyer, C., Polar record of Early Jurassic massive carbon injection. Earth and Planetary
1143 Science Letters 312, p. 102–113 (2011).
1144 Suan, G., Pittet, B., Bour, I., Mattioli, E., Duarte, L.V., Maillot, S., Duration of the Early Toarcian
1145 carbon isotope excursion deduced from spectral analyses: Consequence for its possible
1146 causes. Earth and Planetary Science Letters 267, p. 666–679 (2008).
1147 Tappin, D.R., Chadwick, R.A., Jackson, A.A., Wingfield, R.T.R., Smith, N.J.P., Geology of
1148 Cardigan Bay and the Bristol Channel, United Kingdom Offshore Regional Report, British

Geological Survey, HMSO, p. 107 (1994).
Ullmann, C.V., Hesselbo, S.P., Korte, C., Tectonic forcing of Early to Middle Jurassic seawater Sr/Ca. Geology 41, p. 1211–1214 (2013).
Ullmann, C.V., Thibault, N., Ruhl, M., Hesselbo, S.P., Korte, C., Effect of a Jurassic oceanic anoxic event on belemnite ecology and evolution. Proceedings of the National Academy of Sciences of the United States of America 111, p. 10073–10076 (2014).
van Buchem, F.P.S., Knox, R.W.O'B., Lower and middle Liassic depositional sequences of Yorkshire (UK). Mesozoic and Cenozoic Sequence Stratigraphy of European Basins, SEPM Special Publication No. 60, p. 561–581 (1998).
van Buchem, F.S.P., Melnyk, D.H., McCave, I.N., Chemical cyclicity and correlation of Lower Lias mudstones using gamma ray logs, Yorkshire, UK. Journal of the Geological Society 149, p. 991–1002 (1992).
van Buchem, F.S.P., McCave, I.N., Cyclic sedimentation patterns in Lower Lias mudstones of Yorkshire (GB). Terra Nova 1, p. 461–467 (1989).
van Buchem, F.S.P., McCave, I.N., Weedon, G.P., Orbitally induced small-scale cyclicity in a siliciclastic epicontinental setting (Lower Lias, Yorkshire, UK). In: Boer, P.L., Smith, D.G. (Eds.), Orbital forcing and cyclic sequences. International Association of Sedimentologists Special Publication 19, p. 345–366.
Van de Schootbrugge, B., Bailey, T.R., Rosenthal, Y., Katz, M.E., Wright, J.D., Miller, K.G., Feist-Burkhardt, S., Falkowski, P.G., Early Jurassic climate change and the radiation of organic- walled phytoplankton in the Tethys Ocean. Paleobiology 31, p. 73-97 (2005).
Van der Meer, D.G., Zeebe, R.E., van Hinsbergen, D.J.J., Sluijs, A., Spakman, W., Torsvik, T.H., Plate tectonic controls on atmospheric CO_2 levels since the Triassic. Proceedings of the National Academy of Sciences of the United States of America 111, p. 4380–4385 (2014).
Verati, C., Rapaille, C., Feraud, G., Marzoli, A., Bertrand, H., Youbi, N., $^{40}Ar/^{39}Ar$ ages and duration of the central Atlantic Magmatic Province volcanism in Morocco and Portugal and its relation to the Triassic–Jurassic boundary. Palaeogeography, Palaeoclimatology, Palaeoecology 244, p. 308–325 (2007).
Von Hillebrandt, A.V., Krystyn, L., Kürschner, W.M., Bonis, N.R., Ruhl, M., Richoz, S., Schobben, M.A.N., Urlichs, M., Bown, P.R., Kment, K., McRoberts, C.A., Simms, M., Tomasovych, A., The Global Stratotype Sections and Point (GSSP) for the base of the Jurassic System at Kuhjoch (Karwendel Mountains, Northern Calcareous Alps, Tyrol, Austrie). Episodes 36, p. 162–198 (2013).
Waterhouse, H.K., Regular terrestrially derived palynofacies cycles in irregular marine sedimentary cycles, Lower Lias, Dorset, UK. Journal of the Geological Society, London 156, p. 1113–1124 (1999).
Weedon, G.P., Hemipelagic shelf sedimentation and climatic cycles: the basal Jurassic (Blue Lias) of South Britain. Earth and Planetary Science Letters 76, p. 321-335 (1985/86).
Weedon, G.P., The detection and illustration of regular sedimentary cycles using Walsh power spectra and filtering, with examples from the Lias of Switzerland. Journal of the Geological Society, London 146, p. 133–144 (1989).
Weedon, G.P., Jenkyns, H.C., Coe, A.L., Hesselbo, S.P., Astronomical calibration of the Jurassic time-scale from cyclostratigraphy in British mudrock formations. Philosophical Transactions of the Royal Society of London A 357, p.1787–1813 (1999).
Weedon, G.P., Jenkyns, H.C., Cyclostratigraphy and the Early Jurassic timescale: Data from the Belemnite Marls, Dorset, southern England. Geological Society of America Bulletin 111, p. 1823–1840 (1999).Whiteside, J.H., Olsen, P.E., Eglinton, T., Brookfield, M.E., Sambrotto, R.,N., Compound-specific carbon isotopes from Earth's largest flood basalt eruptions directly linked to the end-Triassic mass extinction. Proceedings of the National Academy of Sciences of the United States of America 107, p. 6721–6725 (2010).
Woodfine, R.G., Jenkyns, H.C., Sarti, M., Baroncini, F., Violante, C., The response of two Tethyan carbonate platforms to the Early Toarcian (Jurassic) oceanic anoxic event: environmental change and differential subsidence. Sedimentology 55, p. 1011–1028 (2008).
Woodland, A.W. (Ed.), The Llanbedr (Mochras Farm) Borehole. Institute of Geological Sciences Report No. 71/18, p. 115 (1971).

Wotzlaw, J.-F., Guex, J., Bartolini, A., Gallet, Y., Krystyn, L., McRoberts, C.A., Taylor, D., Schoene, B., Schaltegger, U., Towards accurate numerical calibration of the Late Triassic: High-precision U-Pb geochronology constraints on the duration of the Rhaetian. Geology 42, p. 571–574 (2014).

FIGURE 1

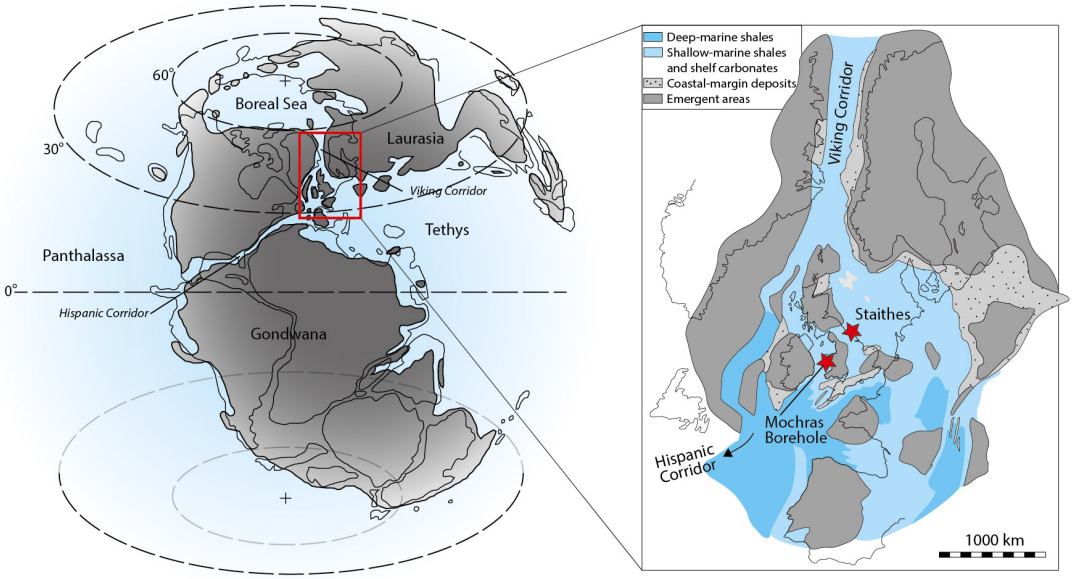
60°
Boreal Sea
Laurasia
30°
Viking Corridor
Tethys
Panthalassa
0°
Hispanic Corridor
Gondwana
Deep-marine shales
Shallow-marine shales and shelf carbonates
Coastal-margin deposits
Emergent areas
Viking Corridor
Staithes
Mochras Borehole
Hispanic Corridor
1000 km

FIGURE 2

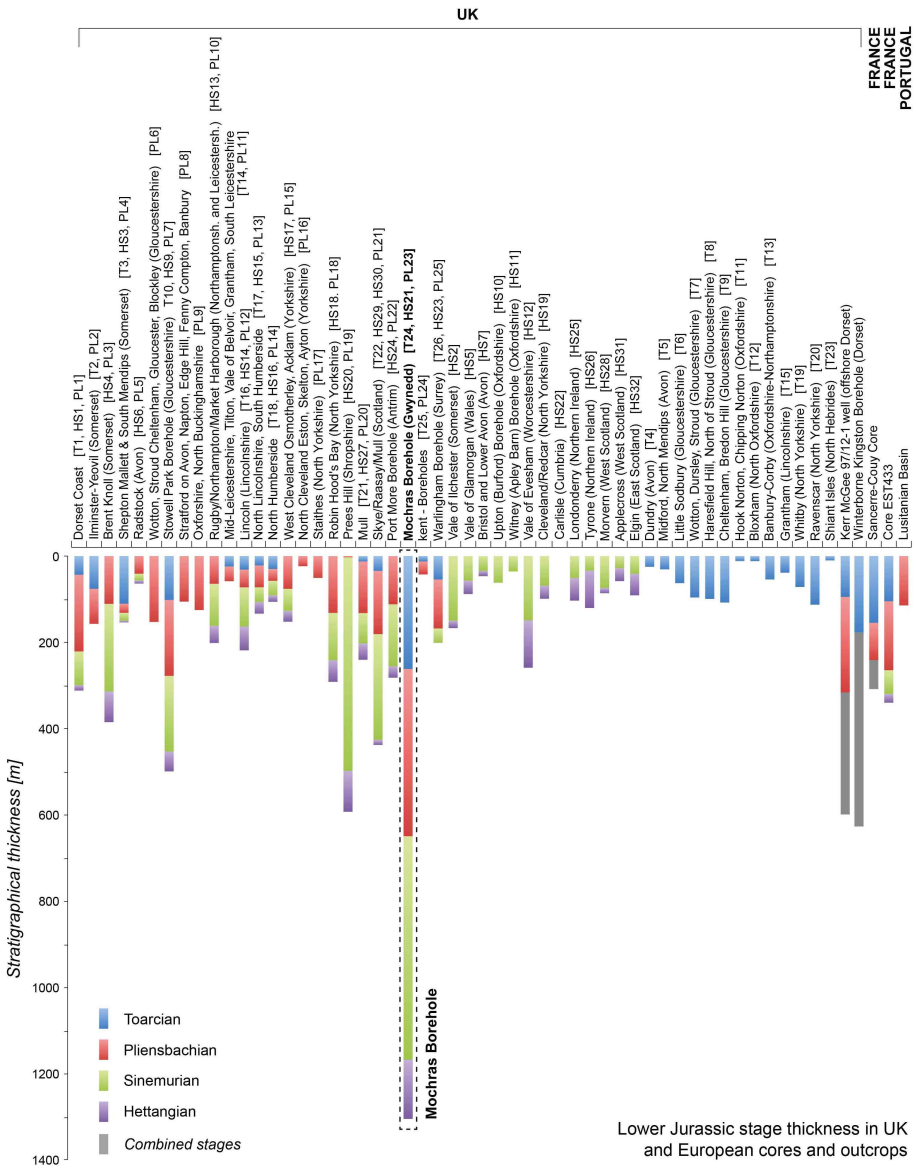
UK
FRANCE
FRANCE
PORTUGAL
Dorset Coast [T1, HS1, PL1]
Ilminster-Yeovil (Somerset) [T2, PL2]
Brent Knoll (Somerset) [HS4, PL3]
Shepton Mallett & South Mendips (Somerset) [T3, HS3, PL4]
Radstock (Avon) [HS6, PL5]
Wotton, Stroud Cheltenham, Gloucester, Blockley (Gloucestershire) [PL6]
Stowell Park Borehole (Gloucestershire) T10, HS9, PL7]
Stratford on Avon, Napton, Edge Hill, Fenny Compton, Banbury [PL8]
Oxfordshire, North Buckinghamshire [PL9]
Rugby/Northampton/Market Harborough (Northamptonsh. and Leicestersh.) [HS13, PL10]
Mid-Leicestershire, Tilton, Vale of Belvoir, Grantham, South Leicestershire [T14, PL11]
Lincoln (Lincolnshire) [T16, HS14, PL12]
North Lincolnshire, South Humberside [T17, HS15, PL13]
North Humberside [T18, HS16, PL14]
West Cleveland Osmotherley, Acklam (Yorkshire) [HS17, PL15]
North Cleveland Eston, Skelton, Ayton (Yorkshire) [PL16]
Staithes (North Yorkshire) [PL17]
Robin Hood's Bay (North Yorkshire) [HS18. PL18]
Prees Hill (Shropshire) [HS20, PL19]
Mull [T21, HS27, PL20]
Skye/Raasay/Mull (Scotland) [T22, HS29, HS30, PL21]
Port More Borehole (Antrim) [HS24, PL22]
Mochras Borehole (Gwynedd) [T24, HS21, PL23]
Kent - Boreholes [T25, PL24]
Warlingham Borehole (Surrey) [T26, HS23, PL25]
Vale of Ilchester (Somerset) [HS2]
Vale of Glamorgan (Wales) [HS5]
Bristol and Lower Avon (Avon) [HS7]
Upton (Burford) Borehole (Oxfordshire) [HS10]
Witney (Apley Barn) Borehole (Oxfordshire) [HS11]
Vale of Evesham (Worcestershire) [HS12]
Cleveland/Redcar (North Yorkshire) [HS19]
Carlisle (Cumbria) [HS22]
Londonderry (Northern Ireland) [HS25]
Tyrone (Northern Ireland) [HS26]
Morvern (West Scotland) [HS28]
Applecross (West Scotland) [HS31]
Elgin (East Scotland) [HS32]
Dundry (Avon) [T4]
Midford, North Mendips (Avon) [T5]
Little Sodbury (Gloucestershire) [T6]
Wotton, Dursley, Stroud (Gloucestershire) [T7]
Haresfield Hill, North of Stroud (Gloucestershire) [T8]
Cheltenham, Bredon Hill (Gloucestershire) [T9]
Hook Norton, Chipping Norton (Oxfordshire) [T11]
Bloxham (North Oxfordshire) [T12]
Banbury-Corby (Oxfordshire-Northamptonshire) [T13]
Grantham (Lincolnshire) [T15]
Whitby (North Yorkshire) [T19]
Ravenscar (North Yorkshire) [T20]
Shiant Isles (North Hebrides) [T23]
Kerr McGee 97/12-1 well (offshore Dorset)
Winterborne Kingston Borehole (Dorset)
Sancerre-Couy Core
Core EST433
Lusitanian Basin
Stratigraphical thickness [m]
0
200
400
600
800
1000
1200
1400
Toarcian
Pliensbachian
Sinemurian
Hettangian
Combined stages
Mochras Borehole
Lower Jurassic stage thickness in UK
and European cores and outcrops

FIGURE 3

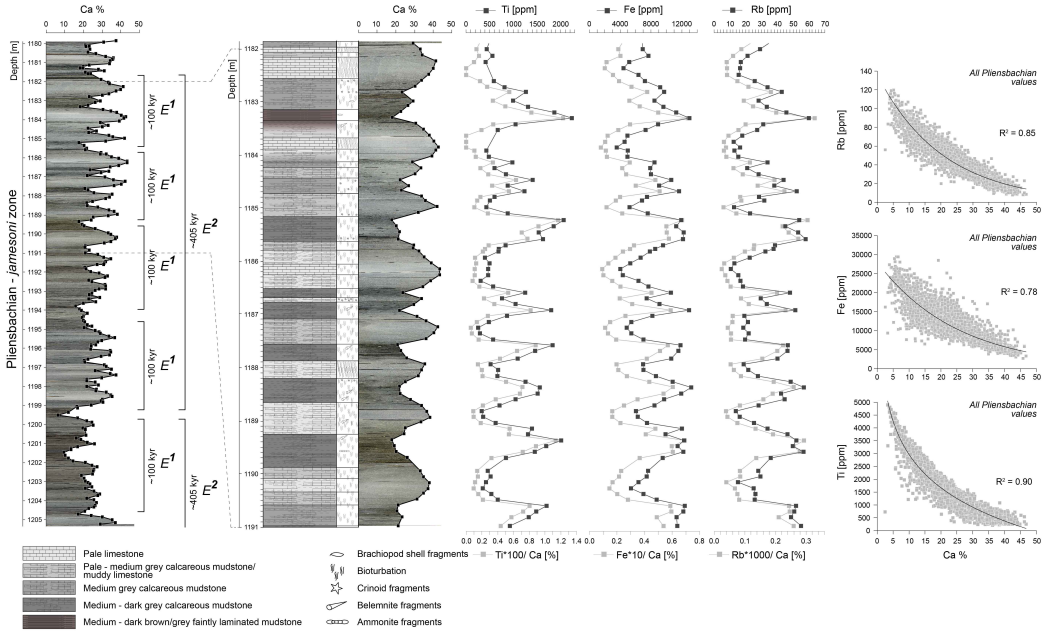
Ca %
Depth [m]
Pliensbachian - jamesoni zone
~100 kyr
E1
~405 kyr
E2
Ti [ppm]
Fe [ppm]
Rb [ppm]
Ti*100/ Ca [%]
Fe*10/ Ca [%]
Rb*1000/ Ca [%]
All Pliensbachian values
R² = 0.85
R² = 0.78
R² = 0.90
Rb [ppm]
Fe [ppm]
Ti [ppm]
Pale limestone
Pale - medium grey calcareous mudstone/ muddy limestone
Medium grey calcareous mudstone
Medium - dark grey calcareous mudstone
Medium - dark brown/grey faintly laminated mudstone
Brachiopod shell fragments
Bioturbation
Crinoid fragments
Belemnite fragments
Ammonite fragments

FIGURE 4

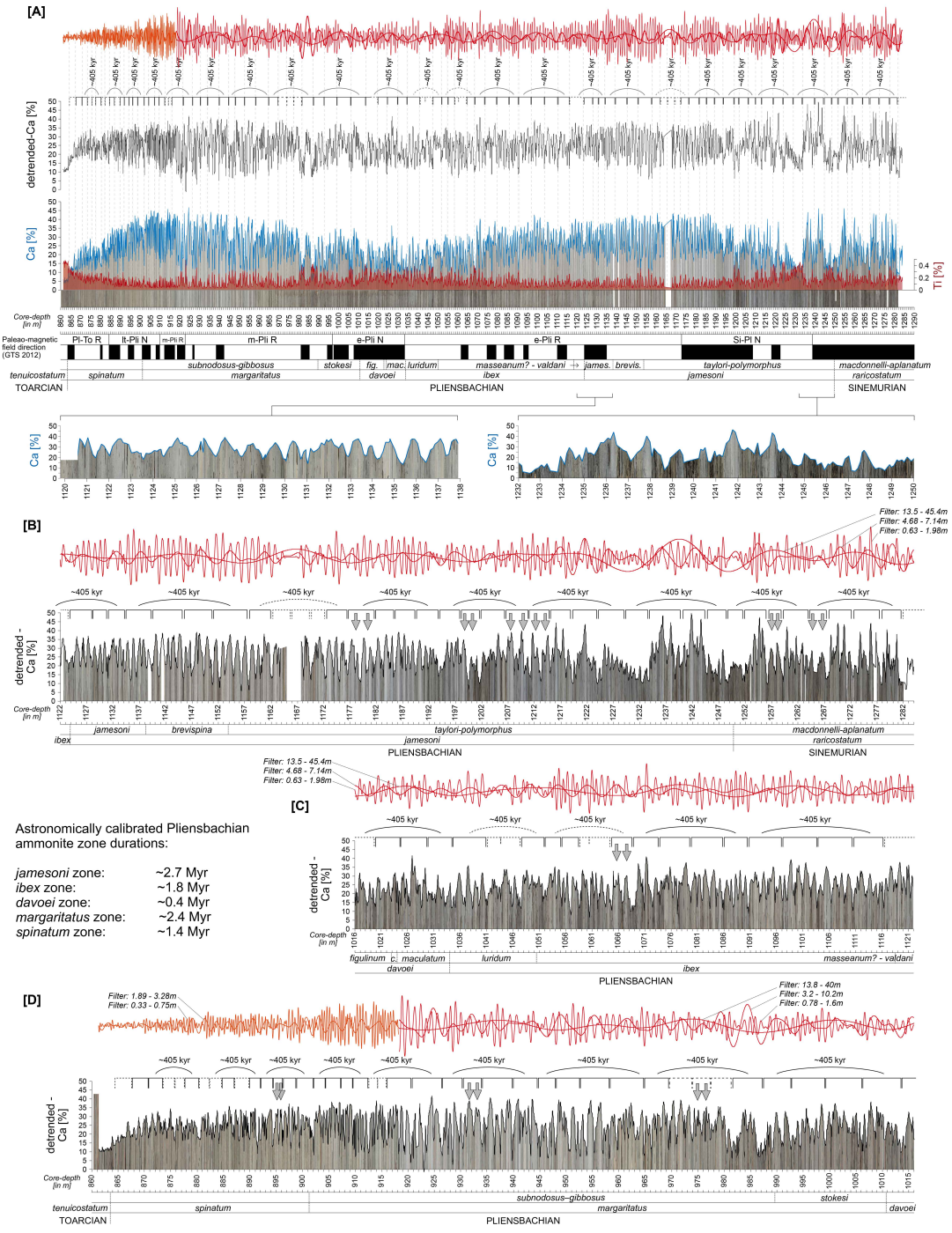

Astronomically calibrated Pliensbachian ammonite zone durations:

jamesoni zone:	~2.7 Myr
ibex zone:	~1.8 Myr
davoei zone:	~0.4 Myr
margaritatus zone:	~2.4 Myr
spinatum zone:	~1.4 Myr

FIGURE 5

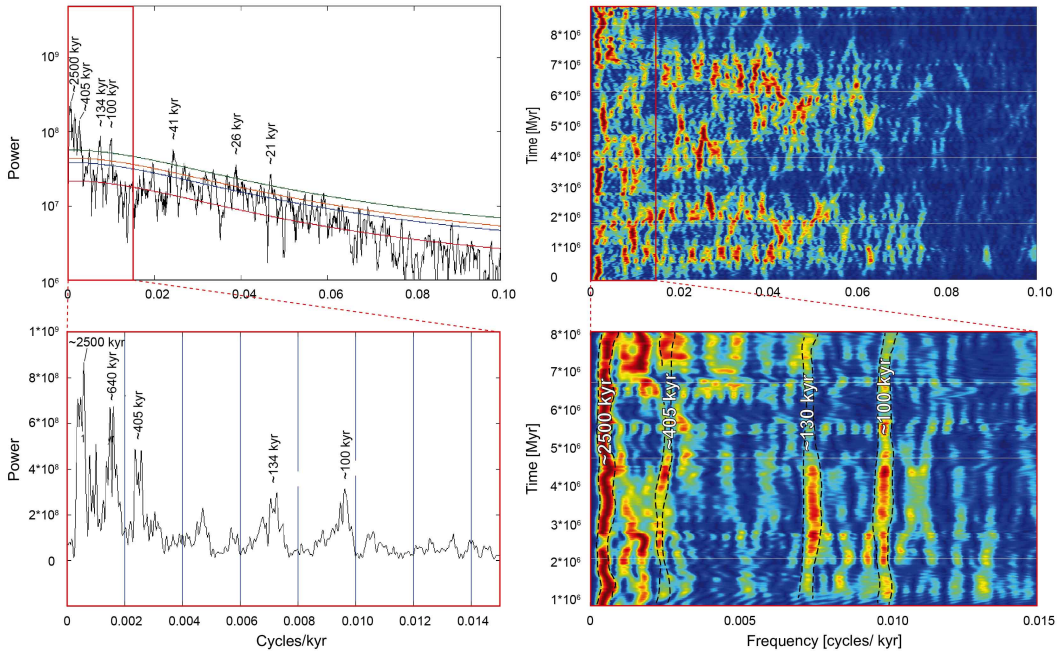
Power
~2500 kyr
~405 kyr
~134 kyr
~100 kyr
~41 kyr
~26 kyr
~21 kyr
Time [Myr]
~640 kyr
Cycles/kyr
Frequency [cycles/ kyr]

FIGURE 6

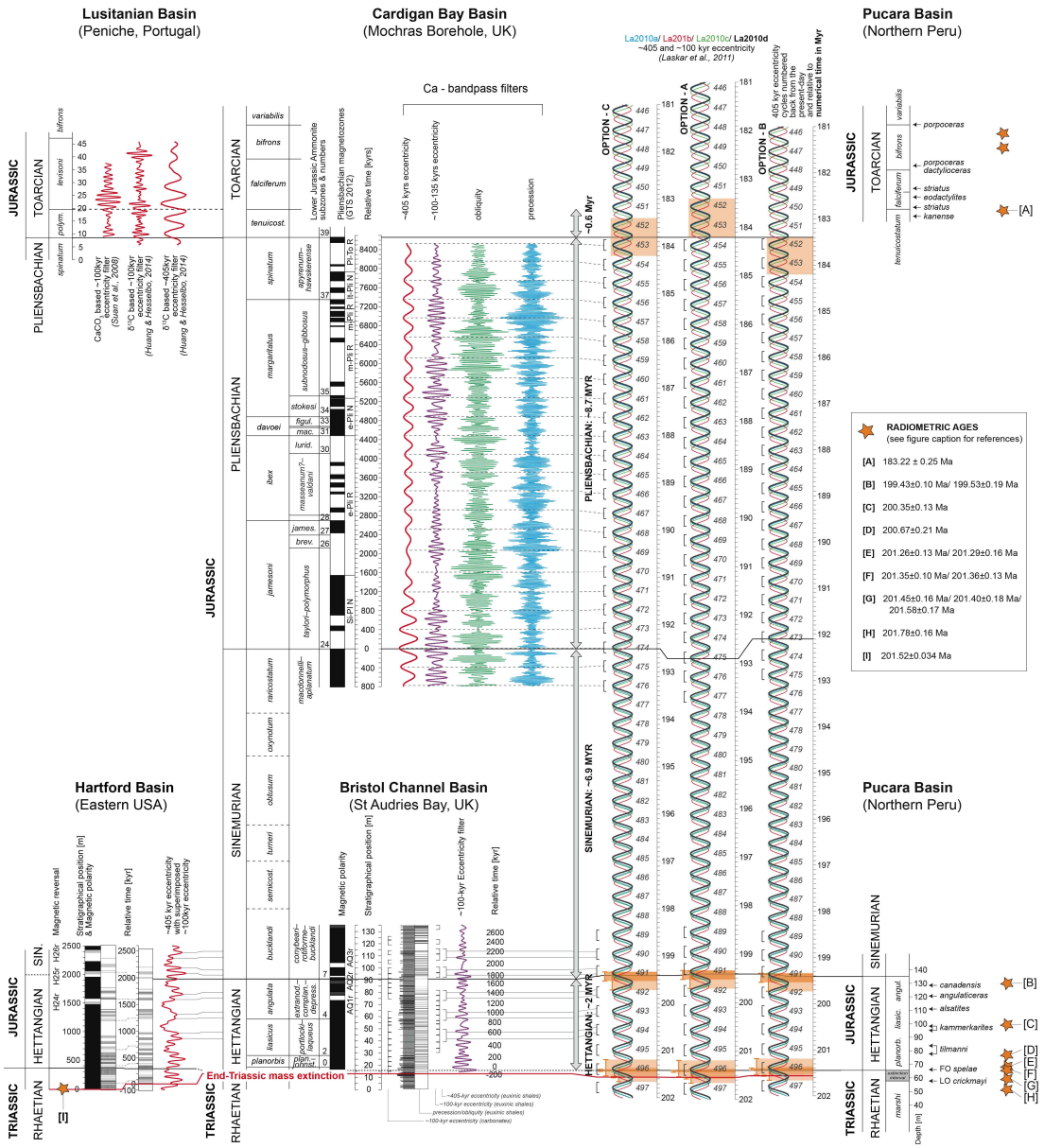
Lusitanian Basin
(Peniche, Portugal)
Cardigan Bay Basin
(Mochras Borehole, UK)
Pucara Basin
(Northern Peru)
Hartford Basin
(Eastern USA)
Bristol Channel Basin
(St Audries Bay, UK)
Pucara Basin
(Northern Peru)
La2010a/ La201b/ La2010c/ La2010d
~405 and ~100 kyr eccentricity
(Laskar et al., 2011)
Ca - bandpass filters
~405 kyrs eccentricity
~100-135 kyrs eccentricity
obliquity
precession
OPTION - C
OPTION - A
OPTION - B
PLIENSBACHIAN: ~8.7 MYR
SINEMURIAN: ~6.9 MYR
HETTANGIAN: ~2 MYR
~0.6 Myr
End-Triassic mass extinction
RADIOMETRIC AGES
(see figure caption for references)
[A] 183.22 ± 0.25 Ma
[B] 199.43±0.10 Ma/ 199.53±0.19 Ma
[C] 200.35±0.13 Ma
[D] 200.67±0.21 Ma
[E] 201.26±0.13 Ma/ 201.29±0.16 Ma
[F] 201.35±0.10 Ma/ 201.36±0.13 Ma
[G] 201.45±0.16 Ma/ 201.40±0.18 Ma/ 201.58±0.17 Ma
[H] 201.78±0.16 Ma
[I] 201.52±0.034 Ma

FIGURE 7

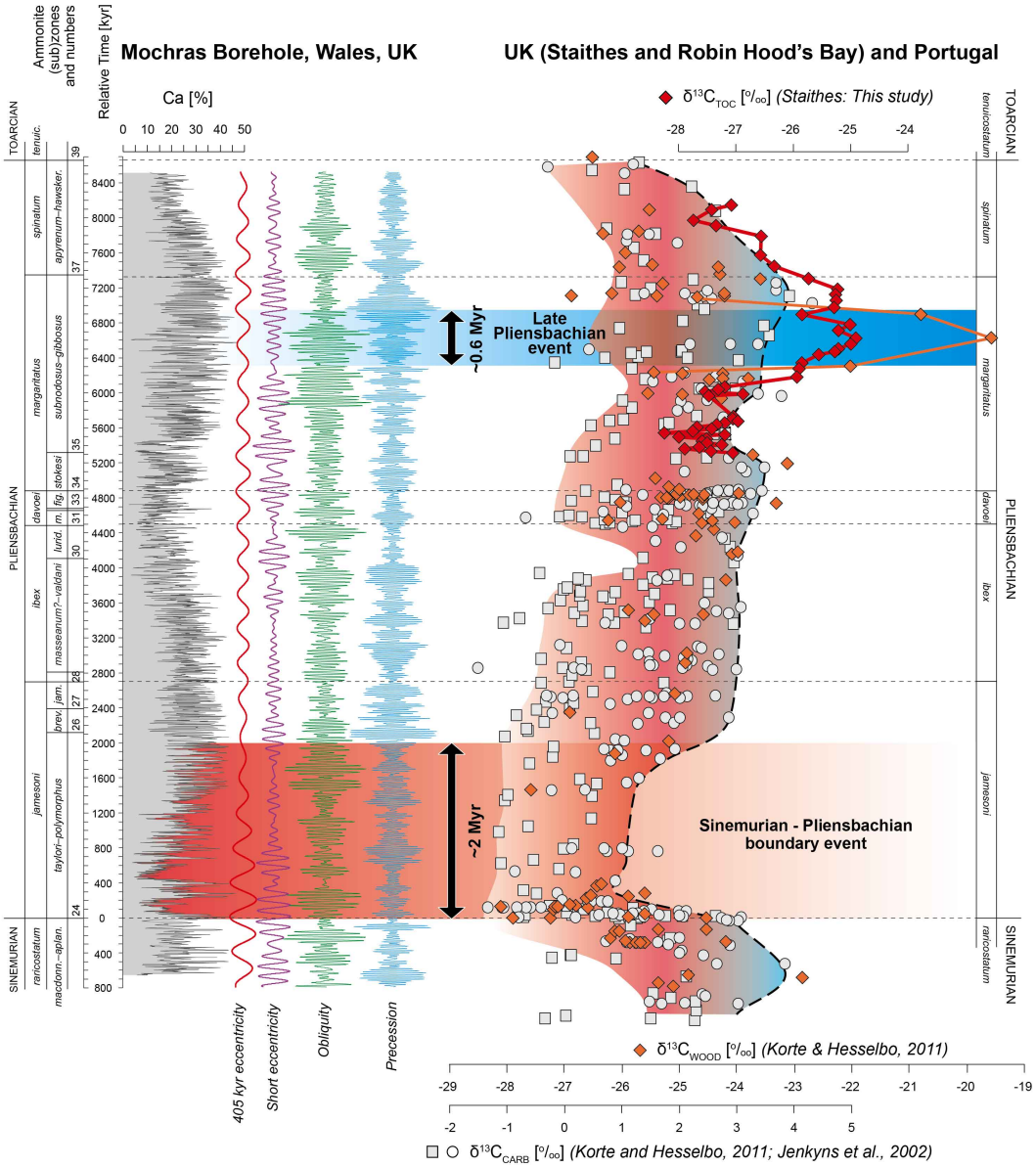
Mochras Borehole, Wales, UK
UK (Staithes and Robin Hood's Bay) and Portugal
Ammonite (sub)zones and numbers
Relative Time [kyr]
Ca [%]
δ13CTOC [‰] (Staithes: This study)
Late Pliensbachian event
~0.6 Myr
~2 Myr
Sinemurian - Pliensbachian boundary event
405 kyr eccentricity
Short eccentricity
Obliquity
Precession
δ13CWOOD [‰] (Korte & Hesselbo, 2011)
δ13CCARB [‰] (Korte and Hesselbo, 2011; Jenkyns et al., 2002)
TOARCIAN
PLIENSBACHIAN
SINEMURIAN

FIGURE 8

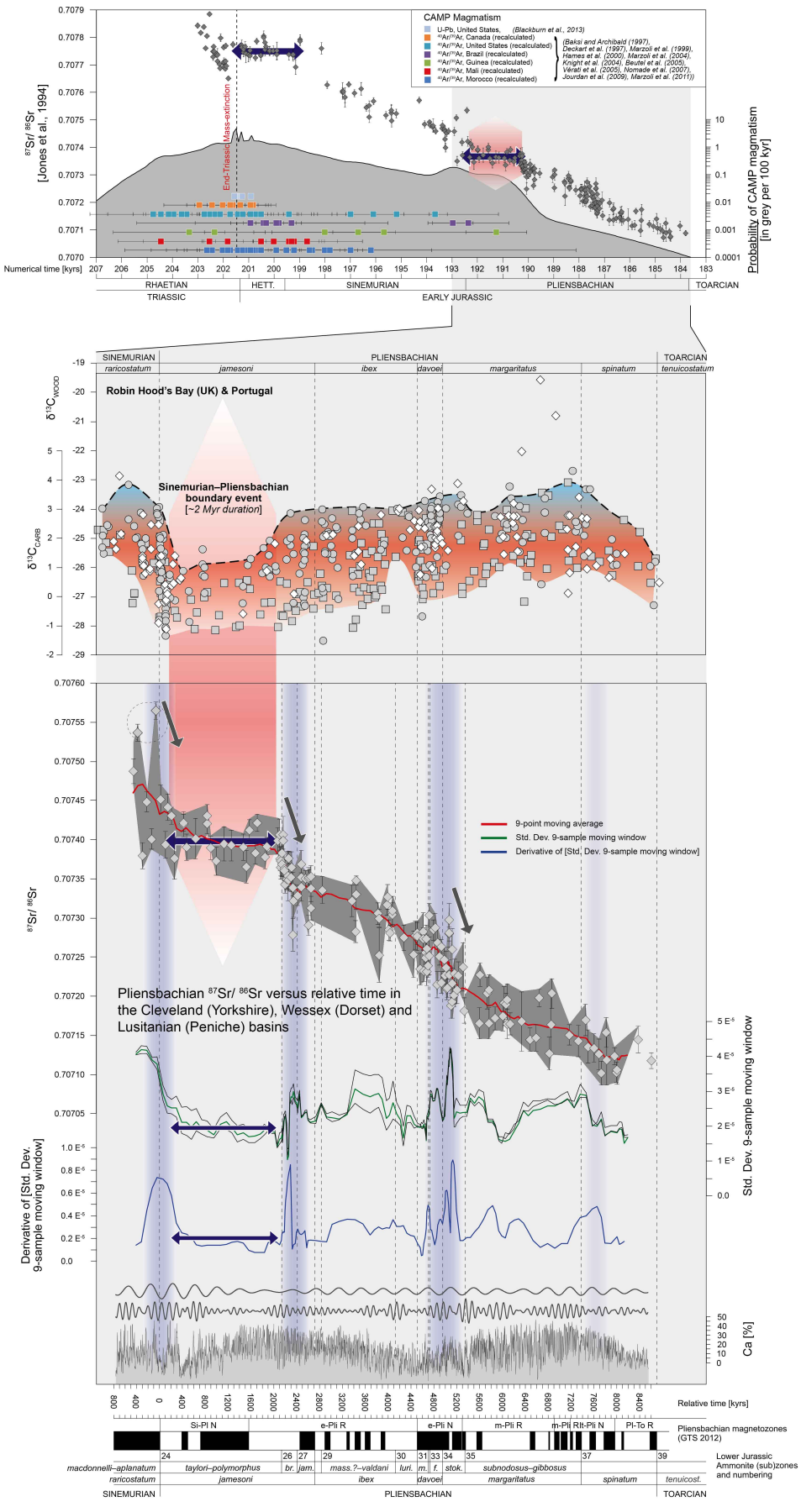
CAMP Magmatism
U-Pb, United States, (Blackburn et al., 2013)
(Baksi and Archibald (1997), Deckart et al. (1997), Marzoli et al. (1999), Hames et al. (2000), Marzoli et al. (2004), Knight et al. (2004), Beutel et al. (2005), Vérati et al. (2005), Nomade et al. (2007), Jourdan et al. (2009), Marzoli et al. (2011))
End-Triassic Mass-extinction
87Sr/ 86Sr [Jones et al., 1994]
Probability of CAMP magmatism [in grey per 100 kyr]
Numerical time [kyrs]
RHAETIAN
HETT.
SINEMURIAN
PLIENSBACHIAN
TOARCIAN
TRIASSIC
EARLY JURASSIC
raricostatum
jamesoni
ibex
davoei
margaritatus
spinatum
tenuicostatum
Robin Hood's Bay (UK) & Portugal
Sinemurian–Pliensbachian boundary event
[~2 Myr duration]
9-point moving average
Std. Dev. 9-sample moving window
Derivative of [Std. Dev. 9-sample moving window]
Pliensbachian 87Sr/ 86Sr versus relative time in the Cleveland (Yorkshire), Wessex (Dorset) and Lusitanian (Peniche) basins
Relative time [kyrs]
Si-Pl N
e-Pli R
e-Pli N
m-Pli R
m-Pli RIt-Pli N
Pl-To R
Pliensbachian magnetozones (GTS 2012)
macdonnelli–aplanatum
taylori–polymorphus
br.
jam.
mass.?–valdani
luri.
m.
f.
stok.
subnodosus–gibbosus
tenuicost.
Lower Jurassic Ammonite (sub)zones and numbering

TABLE 1

Table 1: Early Jurassic Stage and ammonite zone ages and durations

Stage	Ammonite Zone	Base Age [Myr]	Base age: radiometric and astrochronological uncertainty [Myr]	Mochras Borehole: base biostratigraphic uncertainty [Myr]	Duration and biostratigraphic uncertainty [Myr]
	tenuicostatum	183.8	+/-0.4	+0.25	~0.6
Toarcian		**183.8**	**+/-0.4** *(combined astrochr./ radiom. uncertainty)*	**+0.25**	**~8.3**
	spinatum	185.2	+/-0.4 *(extrapolated from above)*	+0.25	~1.4 (+0.25/-0.25)
	margaritatus	187.6	+/-0.4 *(extrapolated from above)*	0	~2.4 (-0.25)
	davoei	188.0	+/-0.4 *(extrapolated from above)*	0	~0.4
	ibex	189.8	+/-0.4 *(extrapolated from above)*	0	~1.8
	jamesoni	192.5	+/-0.4 *(extrapolated from above)*	+0.15	~2.7 (+0.15)
Pliensbachian		**192.5**	**+/-0.4** *(extrapolated from above)*	**+0.15**	**~8.7 (+0.15/-0.25)**
	raricostatum				> 0.8
	oxynotum				
	obtusum				
	turneri				
	semicostatum				
	bucklandi	199.43	+/-0.1 *(radiometric uncertainty)*		> 1.1
Sinemurian		**199.43**	**+/-0.1** *(radiometric uncertainty)*		**6.93 (+0.75/-0.65)**
	angulata	~200.25			~0.82
	liasicus	~201.04			~0.79
	planorbis	~201.35			~0.31
Hettangian	*spelae*	**201.42**	**+/-0.02** *(radiometric uncertainty)*		**1.99 (+/-0.12)**

Supplementary Materials

ASTRONOMICAL CONSTRAINTS ON THE DURATION OF THE EARLY JURASSIC PLIENSBACHIAN STAGE AND GLOBAL CLIMATIC FLUCTUATIONS

Ruhl, M., Hesselbo, S.P., Hinnov, L., Jenkyns, H.C., Xu, W., Riding, J., Storm, M., Minisini, D., Ullmann, C.V., Leng, M.J.

[1] ANALYTICAL METHODS

High-resolution (10–15 cm) elemental concentrations (e.g. Ca, Ti, Fe, Rb, Zr) were obtained by hand-held X-ray fluorescence (XRF) analyses on the slabbed archive half of the Mochras core, from the late Sinemurian *raricostatum* zone (starting at 1284.08 m in the *macdonnelli–aplanatum* subzone) to the Early Toarcian *tenuicostatum* zone (up to a depth of 861.32 m). XRF analyses were conducted with a Thermo Scientific Niton XLT instrument, with a 50-sec measurement window, in soil mode. Long-term drift in measurement values was counteracted by regular internal calibration. Internal measurement uncertainty, partly due to internal calibration and Compton normalization, differs between elements and is reported in Table 1. Long-term drift in analyses was further checked by repeated analysis of the NIST2780 and NIST2709 international reference standards. Repeated analysis of the NIST2780 standard showed for calcium (Ca) an average of 1426 ppm, with a standard deviation (StDev) of 205 ppm and an average internal error of 112 ppm, and for iron (Fe) an average of 28395 ppm, with a standard deviation of 240 ppm and an average internal error of 216 ppm. Repeated analysis of the NIST2709 standard showed for calcium an average of 21130 ppm, with a standard deviation of 362 ppm and an average internal error of 476 ppm, and for Fe an average of 34678 ppm, with a standard deviation of 382 ppm and an average internal error of 454 ppm. Reproducibility of XRF-based calcium concentration data was further confirmed by comparison to Rock-Eval derived calcium carbonate content ($CaCO_3$; calculated from mineral carbon) (Supplementary Figure 1).

Rock-Eval analysis was performed with the Rock-Eval VI unit from Vinci Technologies, at the department of Earth Sciences, University of Oxford. Samples were homogenised and ~50 mg of sample was subsequently analysed by heating (with incremental temperature increases from room temperature to up to 850°C) in the oxidation and pyrolysis ovens. Mineral carbon content was calculated from the $S3_{MINC}$ and S5 peaks, resulting from the CO and CO_2 flux from the sample and analysed by infrared detector. The TOC content was simultaneously obtained in the same sample-run and was calculated from the combined CO and CO_2 fluxes representing the Pyrolysable Carbon (PC: $S1 + S2 + S3_{CO} + S3_{CO2}$) and the Residual Carbon (RC: $S4_{CO} + S4_{CO2}$). Precision and accuracy of the Rock-Eval analyses was checked by regular measurement of the in-house standard SAB134 (a Lower Jurassic shale) and the international reference standard IFP160000. Repeated long-term analyses of the mineral carbon content of the in-house SAB134 standard shows an average of 5.97%, with a StDev of 0.37%. These values include all outliers; performance is generally better, with an average concentration of 6.03% and a StDev of 0.11%. Repeated long-term analyses of the mineral carbon content of the IFP160000 standard shows an average concentration of 3.20%, with a StDev of

0.02% (the mineral carbon concentration of this standard is referenced at 3.26 ± 0.12%). Repeated long-term analyses of the TOC content of the in-house SAB134 standard shows an average of 2.87%, with a StDev of 0.39%. These values include all outliers; performance is generally better, with an average concentration of 2.80% and a StDev of 0.11%. Repeated long-term analyses of the TOC content of the IFP160000 standard showed an average concentration of 3.27%, with a StDev of 0.04% (the TOC content of this standard is referenced at 3.28 ± 0.14%).

Calcium concentration spot-analysis by XRF was performed on the slabbed core, whereas $CaCO_3$ analysis (calculated from the mineral carbon content) by Rock Eval was performed on homogenised 1 cm^3 samples from stratigraphically nearby (within a few cm), but different, depth intervals (Supplementary Figure 1). Despite this minor stratigraphic offset, calculated calcium concentrations from Rock Eval and adjacent XRF measurements still correlate well (with $R^2 > 0.75$) (Supplementary Figure 1). Additionally, minor offsets between the Ca-concentration from XRF analyses and the calculated Ca-concentration, based on the mineral carbon content measured by Rock-Eval, may also derive from the presumption that carbonate minerals are all associated with calcite, as $CaCO_3$. Some of the carbonate minerals in the host-rock may exist as dolomite or siderite, rather then calcium carbonate. The combined internal error on XRF-based Ca analysis and Rock Eval-based $CaCO_3$ analysis was at any time 1–2 orders of magnitude smaller than the observed variability between the mudstone/marl and the calcareous mudstone/limestone in the Mochras core.

Analysis of $\delta^{13}C_{TOC}$ was performed on decarbonated and homogenized Upper Pliensbachian outcrop samples from Staithes (Yorkshire; locality described in Korte and Hesselbo (2011)). One gram of homogenized sample material was decarbonated twice with 3 M HCl in a warm water bath at 80 °C for 5 hours. The sample was subsequently rinsed three times with Milli-Q water to reach neutral *p*H levels. Between 1–10 mg of decarbonated sample (aiming for ~25 μg pure carbon) was then weighed into 8×5 mm thin capsules for $\delta^{13}C_{TOC}$ analyses. $\delta^{13}C_{TOC}$ analyses were performed at the School of Archaeology (University of Oxford) and at the Stable Isotope Laboratory at the Open University (Milton Keynes, UK), with a Thermo Scientific Flash 2000 HT Elemental Analyser (EA) coupled to a Thermo Scientific MAT253 isotope ratio mass spectrometer via a Conflo IV open split interface. The Thermo Scientific Flash 2000 HT EA has a MAS2000 carousel and, between the carousel and the EA, sits a Thermo No Blank Device (NBD), allowing for the single sample purging with helium. The EA is also equipped with a Thermal Conductivity Detector (TCD). Automated dilution of sample gas with the Conflo IV open split interface allowed for high dynamic range of C (+N) content and controlled the introduction of the reference gases. Analytical precision at the Open University was checked by routine analysis of three internal and referenced laboratory standards, urea 020914MAG, glutamic acid light and Alanine-A, which give measured average $\delta^{13}C$ values of –43.9‰, –25.1‰ and –22.2‰, respectively, with standard deviations of 0.3‰, 0.2‰ and 0.1‰. Analytical precision for $\delta^{13}C_{TOC}$ analyses at the Universty of Oxford was checked by routine analysis of the Alanine-B international reference standard, which showed average $\delta^{13}C_{TOC}$ of –26.9‰, with a StDev of 0.1‰ (the Alanine-B standard is referenced at -26.65‰). Isotope ratios are reported in standard delta notation relative to Vienna PDB.

[2] SUPPLEMENTARY FIGURE CAPTIONS

SUPPLEMENTARY FIGURE 1 Comparison of hand-held X-ray fluorescence (blue) and Rock Eval-based (red) calcium (Ca) concentrations in a selected part of the Mochras Core. Note that analyses are not performed on the same stratigraphic sample-depths. Black dots give the stratigraphic difference in centimetre between a Rock-Eval measurement and the stratigraphically nearest hand-held XRF analyses. Despite the Rock-Eval and hand-held XRF analyses on stratigraphically different (but nearby) samples, the obtained Ca concentrations correlate well, with an R^2 of ~0.75.

SUPPLEMENTARY FIGURE 2 XRF-derived Ca-concentrations across the Sinemurian-Pliensbachian boundary are plotted on top of the stacked core-photos showing clear correlation between elevated Ca-concentrations and lighter-grey sedimentary horizons. Mineral carbon content, derived by Rock-Eval analyses, closely matches fluctuations in Ca-concentrations. TOC and HI values, derived from Rock-Eval analyses negatively correlate to Ca and mineral-carbon concentrations.

SUPPLEMENTARY FIGURE 3 Scanning Electron Microscopy (SEM) backscatter pictures of (A) a calcareous mudstone (depth: 842.04 m core-depth below surface) with fine silt-sized detrital calcite grains circled in red dashed line and (B) a limestone interval (depth: 807.19 m core-depth below surface), with a massive calcium carbonate matrix and some replacement by quartz.

SUPPLEMENTARY FIGURE 4 Multi-taper (MTM) spectral analyses of the obtained XRF elemental (Ca) depth series using the Astrochron (R (3.1.2) Package for astrochronology, version 0.3.1) toolkit (Meyers, 2014). (A) Multi-taper (MTM) power spectrum of the complete Pliensbachian (uppermost *raricostatum* to lowermost *tenuicostatum*) Ca record, showing clear dominance of the >150m periodicity. (B) Multi-taper (MTM) power spectrum of the complete detrended (high band-pass filter (<150m)) Pliensbachian (uppermost *raricostatum* to lowermost *tenuicostatum*) Ca-record. (C) Multi-taper (MTM) power spectrum of the detrended (high band-pass filter (<150m)) uppermost *raricostatum* to lower *margaritatus* Ca-record. (D) Multi-taper (MTM) power spectrum of the detrended (high band-pass filter (<150m)) upper *margaritatus* to lowermost *tenuicostatum* Ca record. Note the order of magnitude differences in Linear Power for the MTM Power estimates, especially for Figure D.

SUPPLEMENTARY FIGURE 5 Multi-taper (MTM; 3π) spectral analyses of the obtained XRF elemental (Fe and Ca) time series using the Astrochron (R (3.1.2) Package for astrochronology, version 0.3.1) toolkit (Meyers, 2014), with robust red noise models (Mann and Lees, 1996). The elemental Fe record was first manipulated to give uniform sample spacing using linear interpolation. Initial spectral analysis was performed with AnalySeries on a detrended data-series (with low band-pass filtering to remove >150 m periodicities). Dominant spectral components (Supplementary Figure 3) were subsequently filtered from the data series and compared to the visually defined precession and short- and long-eccentricity periodicities (Figure 3). The elemental Ca record in the depth domain was subsequently converted to the time domain following the observed 405 kyr eccentricity cycles. The multi-taper (MTM; 3π) spectral analyses of the obtained elemental (Fe and Ca) time-series show dominant and significant peaks at precession, obliquity, and short- and long-period eccentricity. MTM power estimates, AR1 confidence level estimates and harmonic test confidence level estimates are performed with the Astrochron (R (3.1.2) Package for astrochronology, version 0.3.1) toolkit (Meyers, 2014). An independent check of the dominant spectral components is

performed with AnalySeries 2.0.8 (Paillard et al., 1996), giving a 80% confidence interval (grey).

SUPPLEMENTARY FIGURE 6 Precession (blue), obliquity (green), 100–135 kyr eccentricity (purple) and 405 kyr eccentricity (red) band-pass filters, reflecting frequency intervals in the MTM power spectra (Supplementary Figure 4) of the detrended (high band-pass) Fe and Ca time series.

SUPPLEMENTARY FIGURE 7 Comparison of the Pliensbachian stratigraphic depth record with the obtained Pliensbachian time series shows a pronounced 40–60% decrease in sedimentation rate in the upper *margaritatus* ammonite zone (starting at ~918m core depth). Lower Jurassic (top Sinemurian to base Toarcian) ammonite genera occurrence is based on Woodland (1971). Blue bars represent the occurrence of ammonite genera, with a specific genus occurring within a 20 feet (6.096m) window (Woodland, 1971). Minor refinements on ammonite zone boundary positions are based on Copestake and Johnson (2014), which are followed here. Many ammonite (sub)zone boundaries are constrained by first and last occurrences of ammonite genera. Some (sub)zone boundaries are potentially less well constrained, as recognized by a grey bar.

SUPPLEMENTARY FIGURE 8 Lower Pliensbachian (*jamesoni* ammonite zone) $^{87}Sr/^{86}Sr$ data plotted in time in kyrs, (A) based on the Mochras-core derived Pliensbachian time-scale as presented in Figure 8 of the main-text, (B) based on the Belemnite Marls (Dorste, UK) derived Lower Pliensbachian time-scale as presented in Weedon and Jenkyns (1999), and (C) assuming equal duration of Pliensbachian ammonite zones. The Early Pliensbachian $^{87}Sr/^{86}Sr$ record in the time-domain shows a plateau, with relatively constant values, throughout the *taylori-polymorphus* ammonite subzones, followed by a rapid drop in the *brevispina* ammonite subzone, based on both the Mochras and the Belemnite Marl derived time-scales. (D) MTM Power spectrum of the tuned *jamesoni*-ammonite zone % Ca-record of the Mochras core, based on the Mochras-time-scale (this study), and (E) the tuned *jamesoni*-ammonite zone % Ca-record of the Mochras core, based on the Belemnite Marl time-scale of Weedon and Jenkyns (1999), following similar methods and parameters as presented in Supplementary Figures 4 and 5. (D) Clear peaks on expected astronomical frequencies, while peaks in (E) show no resemblance to astronomical frequencies as known from the geological record and astronomical solutions. This inconsistency suggests that the Lower Pliensbachian time-scale based on the Belemnite Marls is incorrect, which can be largely explained by the observed sedimentary hiatuses at the base of the *jamesoni* ammonite subzone and possibly within the *brevispina* ammonite subzone.

[3] REFERENCES

Cope, J.C.W., Getty, T.A., Howarth, M.K., Morton, N., Torrens, H.S., A correlation of Jurassic rocks in the British Isles, Part One: Introduction and Lower Jurassic. Geol. Soc. Lond., Special report No. 14 (1980).

Copestake, P., Johnson, B., Lower Jurassic Foraminifera from the LLanbedr (Mochrad Farm) Borehole, North Wales, UK. Monograph of the Palaeontographical Society, London: 1–403 (2014).

Ivimey-Cook, H.C., Stratigraphical Palaeontology of the Lower Jurassic of the Llanbedr (Mochras Farm) Borehole. In: Woodland, A.W. (Ed). The Llanbedr (Mochras Farm) Borehole. Institute of Geological Sciences Report No. 71/18, p. 87–92 (1971).

Lorenz, J., Gely, J.-P., Interpretation sequentielle du Jurassique Inferieur et moyen du sud du Basin Parisien a partir des correlations diagraphiques calees sur le forage de Couy (Cher, France). Geobios 17, p. 597–604 (1994).

Ainsworth, N.R., Riley, L.A., Triassic to Middle Jurassic stratigraphy of the Kerr McGee 97/12-1 exploration well, offshore southern England. Marine and Petroleum Geology 27, p. 853–894 (2010).

Brigaud, B., Vincent, B., Carpentier, C., Robin, C., Guillocheau, F., Yven, B., Huret, E., Growth and demise of the Jurassic carbonate platform in the intracratonic Paris Basin (France): Interplay of climate change, eustasy and tectonics. Marine and Petroleum Geology 53, p. 3–29 (2014).

Mattioli, E., Plancq, J., Boussaha, M., Duarte, L.V., Pittet, B., Calcareous nannofossil biostratigraphy: new data from the Lower Jurassic of the Lusitanian Basin. Comunicacoes Geologicas 100, p. 69–76 (2013).

Ivimey-Cook, H.C., Biostratigraphy of the Lower Jurassic and Upper Triassic (Rhaetian) rocks of the Winterborne Kingston borehole, Dorset. Report of the Institute of Geological Sciences (1982).

Weedon, G.P., Jenkyns, H.C., Cyclostratigraphy and the Early Jurassic timescale: Data from the Belemnite Marls, Dorset, southern England. Geological Society of America Bulletin 111, p. 1823–1840 (1999).

Whittaker, A., Green, G.W., Geology of the country around Weston-super-Mare. Mem. Geol. Surv. G.B. (1983).

Woodland, A.W. (Editor). 1971. The Llanbedr (Mochras Farm) Borehole. Rep. No. 71/18, Inst. geol. Sci. 115 pp.

Meyers, S.R. (2014), Astrochron: An R Package for Astrochronology (Version 0.3.1).

Mann, M.E., Lees, J.M., Robust estimation of background noise and signal detection in climatic time series. Climatic Change 33, p. 409–445 (1996).

Paillard, D., L. Labeyrie and P. Yiou, Macintosh program performs time-series analysis, *Eos Trans. AGU,* 77: 379 (1996).

SUPPLEMENTARY FIGURE 1

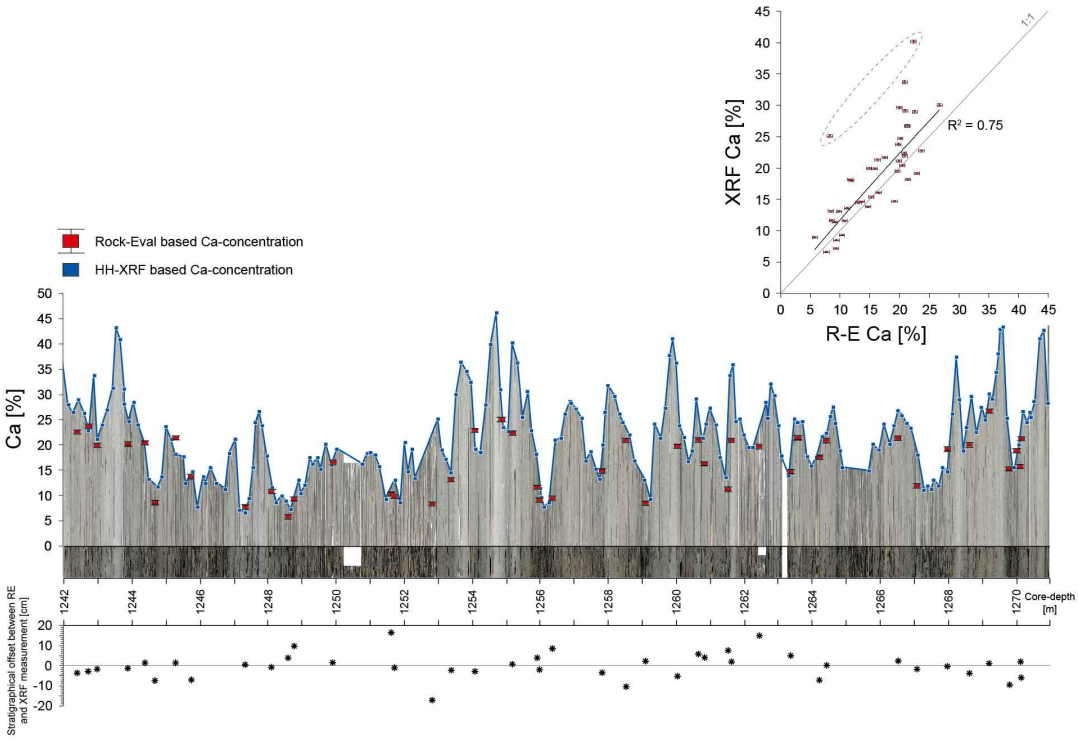

SUPPLEMENTARY FIGURE 2

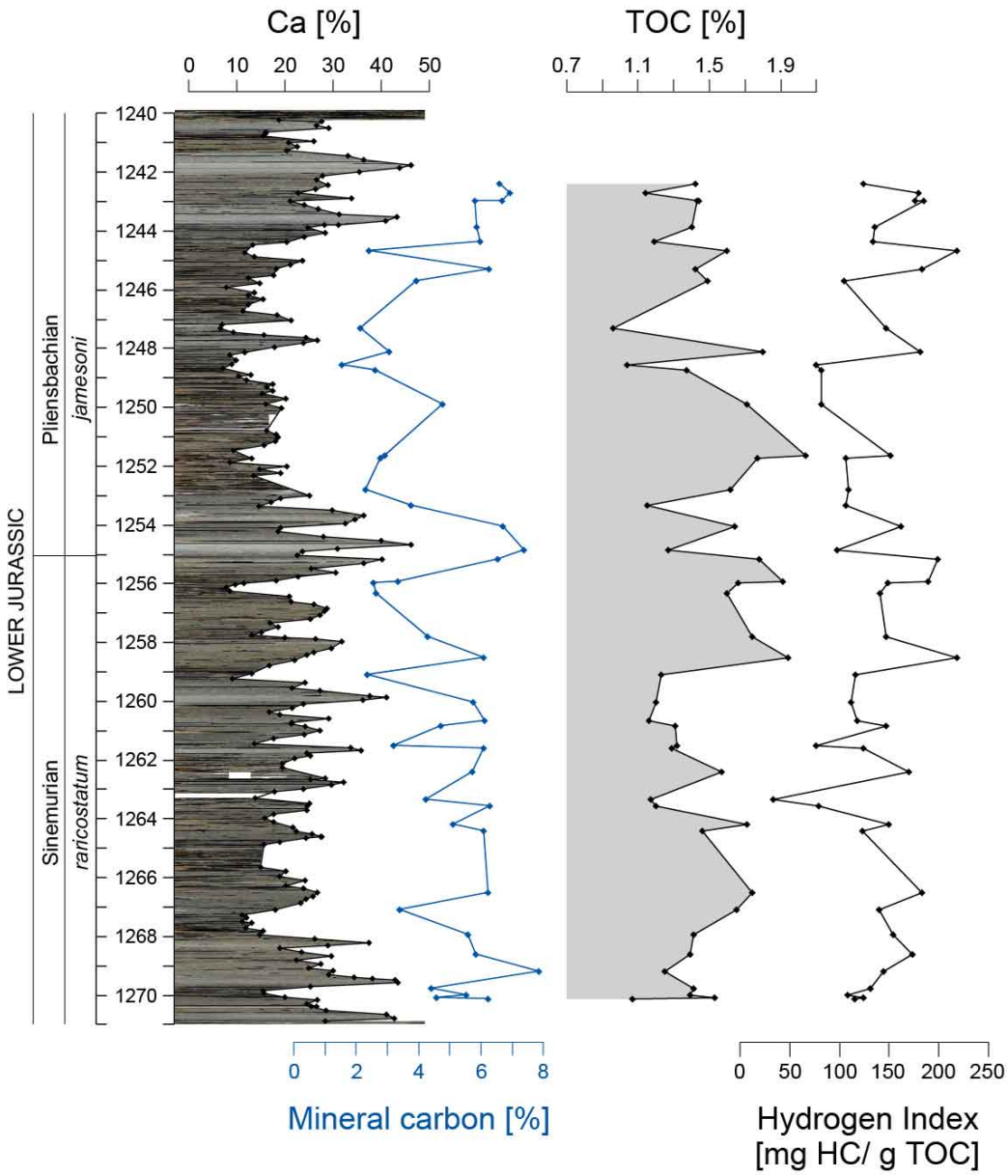

SUPPLEMENTARY FIGURE 3

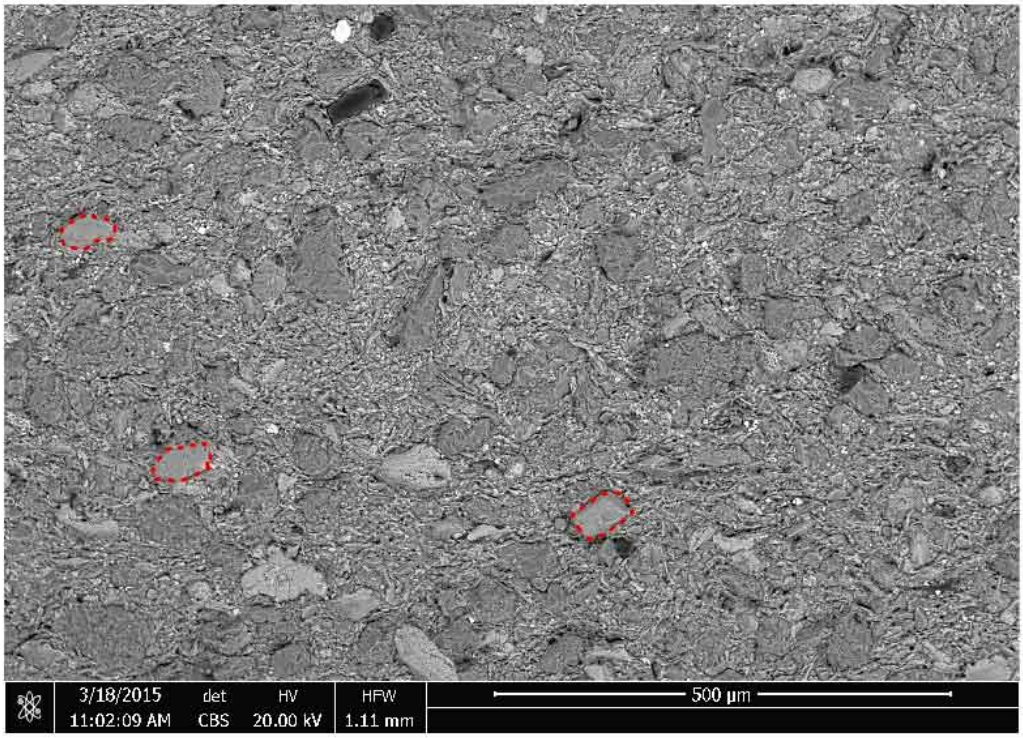

A: Fine silty sized detrital calcite grains circled in red dashed line

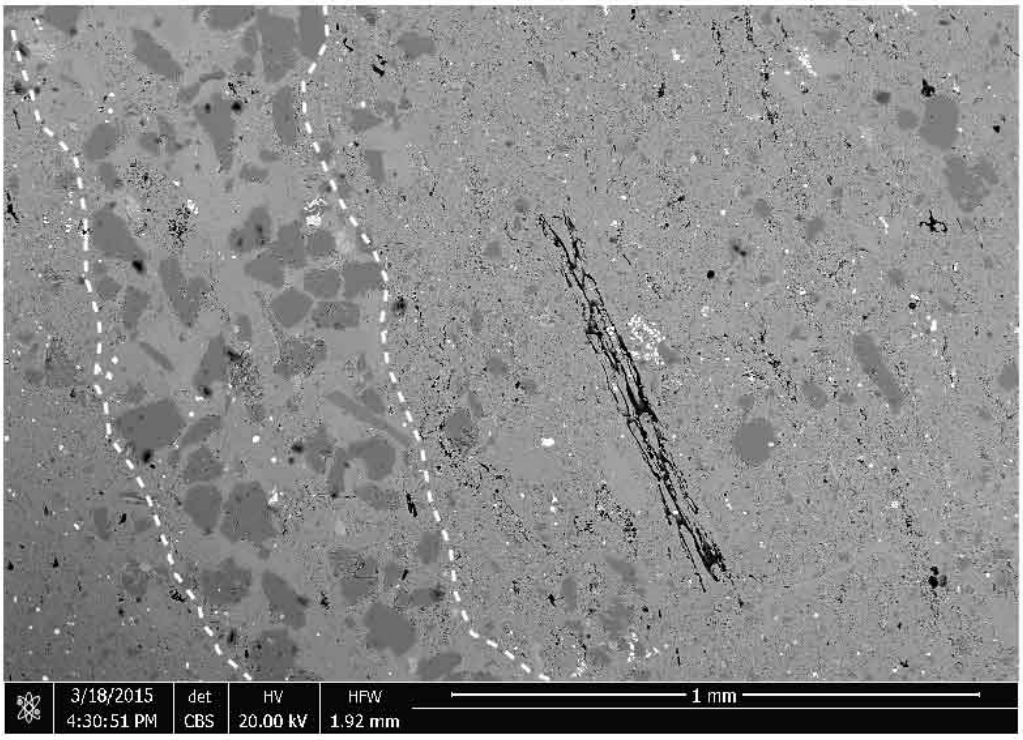

B: Fossil-shell fragment (marked by the white dashed line), which is partly replaced by quartz. The shell fragment and a woody clast (in black) are embedded in a likely early diagenetic massive calcium carbonate matrix.

SUPPLEMENTARY FIGURE 4

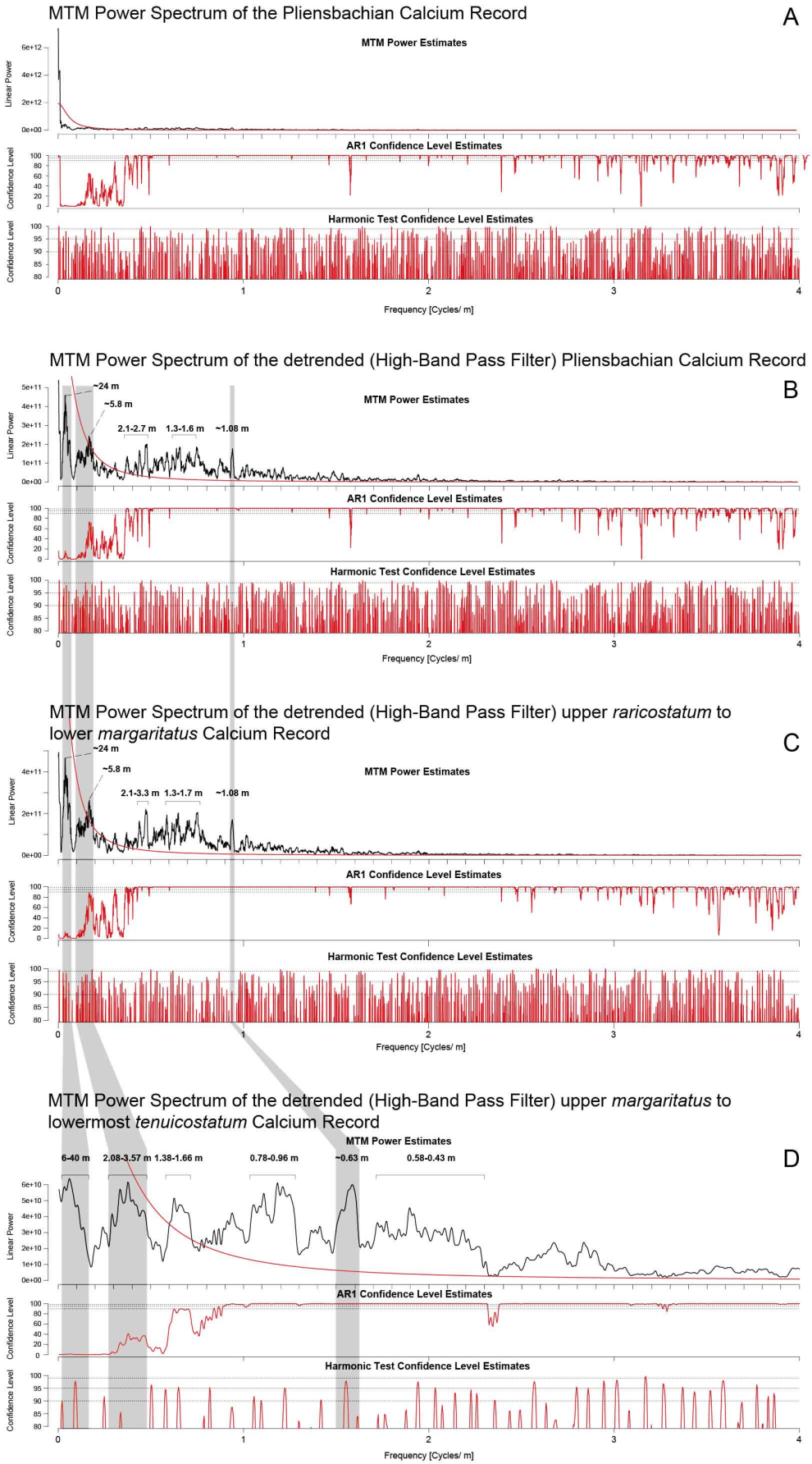

SUPPLEMENTARY FIGURE 5

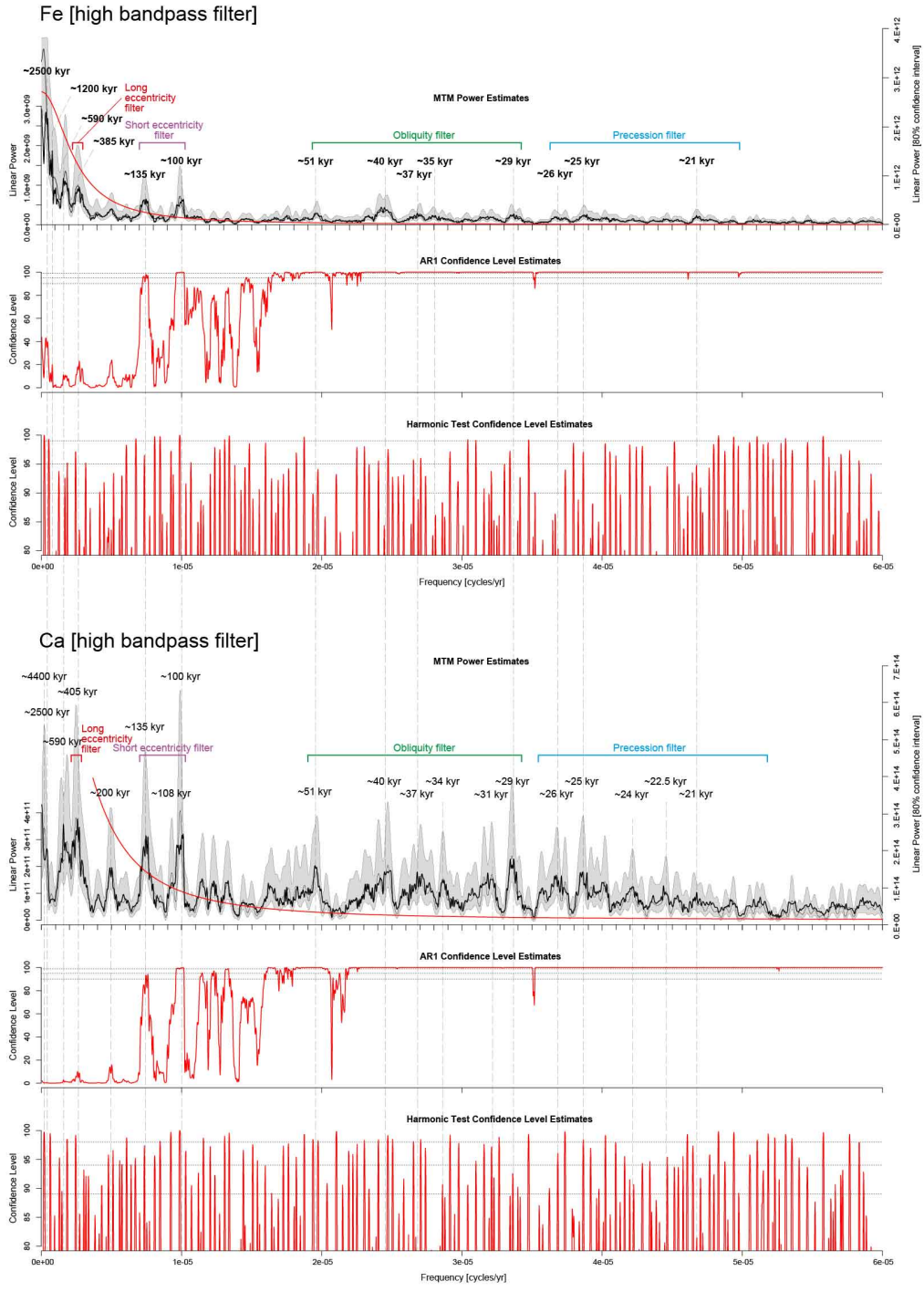

SUPPLEMENTARY FIGURE 6

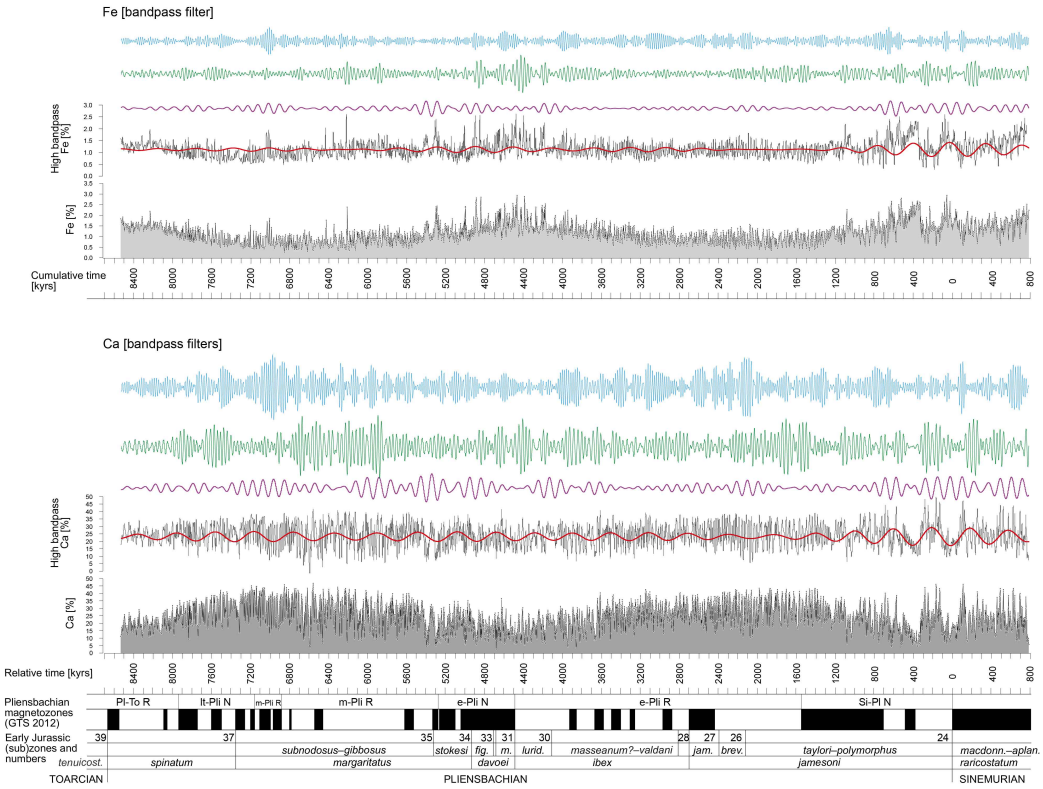

SUPPLEMENTARY FIGURE 7

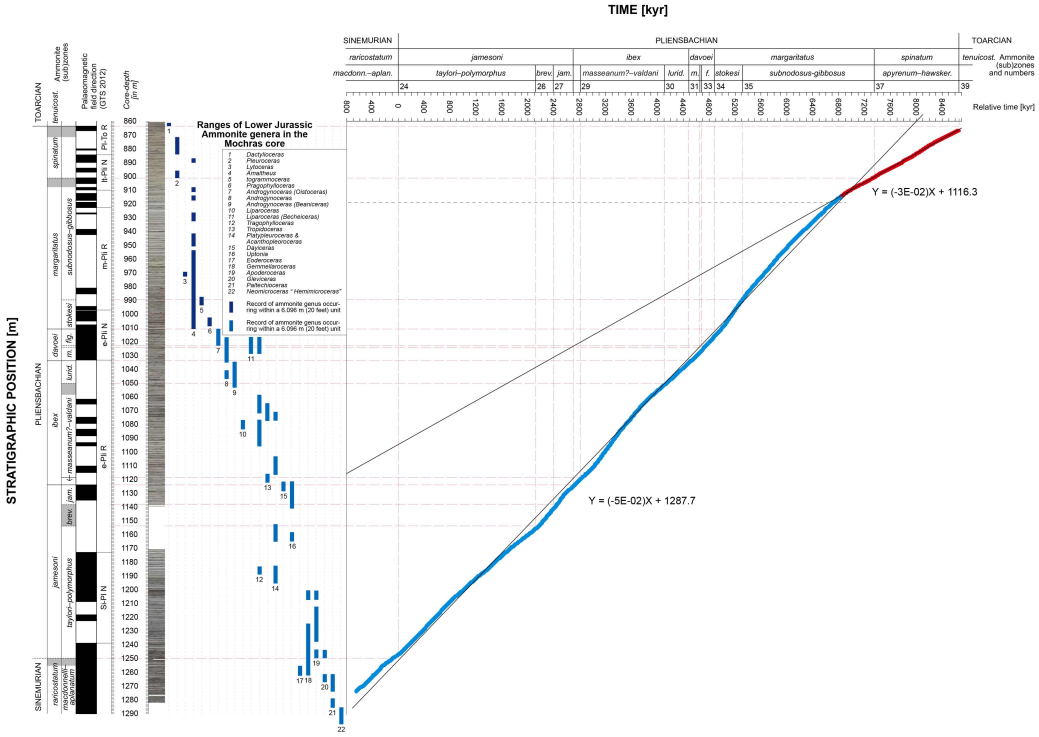

SUPPLEMENTARY FIGURE 8